



TECHNISCHE
UNIVERSITÄT
WIEN
Vienna University of Technology

Diplomarbeit

Improving MRSI Spectral Quality using High-Resolution B0 Inhomogeneity Maps

Ausgeführt am Atominstitut
der Technischen Universität Wien

unter der Anleitung von
Em.Univ.Prof. Dipl.-Ing. Dr.techn. Gerald Badurek
Assoc. Prof. Priv.-Doz. Dipl.-Ing. Dr. Wolfgang Bogner

durch
Stanislav Motyka
Bennogasse 14A/3
1080 Wien

Datum

Unterschrift

Declaration of Authorship

I, Stanislav Motyka, declare that this thesis titled, “Improving MRSI Spectral Quality using High-Resolution B0 Inhomogeneity Maps” and the work presented in it are my own. I confirm that:

Signed:

Date:

Vienna University of Technology

Abstract

Faculty of Physics

Master of Science

**Improving MRSI Spectral Quality using High-Resolution B0
Inhomogeneity Maps**

by Stanislav Motyka

English:

In Magnetic Resonance Spectroscopic Imaging (MRSI) inhomogeneities of the static magnetic field (B_0) cause degradation of spectral quality. The aim of the thesis is to implement post processing methods to improve spectral quality by using additionally acquired high resolution B_0 maps. For this purpose two methods were implemented. The first method suggests B_0 correction in Overdiscrete MRSI (odMRSI) reconstruction in which the MRSI dataset is interpolated by k-space zero filling to match the resolution of the B_0 inhomogeneity map. After the B_0 correction the subvoxels of the interpolated MRSI data are averaged to reach the initial resolution.

The second method, called Spectral Resolution Amelioration by Deconvolution (SPREAD), suggests to estimate lineshape profiles of each voxel from the B_0 inhomogeneities map and to simulate the acquisition of the lineshape profiles at the resolution of the original MRSI dataset. Then spectral deconvolution in time domain is performed between the measured MRSI data and the simulated lineshape profiles. odMRSI reconstruction mainly increases the signal-to-noise ratio (SNR) by decorrelating the spectral noise between subspectra in the interpolation step. SPREAD increases spectral resolution by reduction of linebroadening caused by B_0 inhomogeneities.

Both methods were first validated in simulations and then applied on phantom and in-vivo data. If the outputs of the two methods improve spectral quality significantly they can be used as valuable part of the established postprocessing pipeline. Ultimately, increased SNR can be traded for reduced acquisition time, higher spatial resolutions or to detect low abundant metabolites more confidently.

Our results validated a previous report that odMRSI improved the spectral properties (higher SNR). odMRSI reconstruction was robust against influences from low SNR and can be even based on the shifts maps obtained from MRSI data themselves. This means that the odMRSI can be applied with no additional acquisition time. However, this spectral quality improvement was not translated into better metabolic maps as obtained via spectral quantification. Rather this suggests that the improvement of the spectral properties is just “cosmetic”. In contrast, SPREAD was capable to improve spectral properties only in a situation with high SNR, which is not present in clinical reality.

Based on this we conclude that both SPREAD and odMRSI reconstruction are both not able to provide metabolic maps of improved quality in a (clinical) in vivo setting.

Deutsch:

In der Magnetresonanz-Spektroskopiebildgebung (MRSI) führen Inhomogenitäten im statischen Magnetfeld (B_0) zu einer Verschlechterung der spektralen Qualität. Das Ziel dieser Diplomarbeit war es deshalb eine Nachverarbeitungsmethode zu implementieren, welche die spektrale Qualität durch zusätzlich akquirierte hochaufgelöste B_0 Bilder verbessert.

Hierfür wurden zwei Methoden implementiert. Die erste Methode basiert auf einer B_0 Korrektur mittels Überdiskretisierter MRSI (odMRSI) Rekonstruktion, in welcher die MRSI Datensätze im k -Raum durch Zerofilling interpoliert werden, sodass sie der Auflösung der B_0 Inhomogenitätsbilder entsprechen. Nach der B_0 Korrektur werden die Subvoxel der interpolierten MRSI Daten gemittelt, sodass die ursprüngliche Auflösung wieder erreicht wird.

Die zweite Methode, genannt Spectral Resolution Amelioration by Deconvolution (SPREAD), schlägt vor, dass die Profile der spektralen Resonanzen in jedem Voxel durch eine zusätzliche B_0 Map abgeschätzt werden und die im originalen MRSI Datensatz gemessenen spektralen Resonanzlinien simuliert werden können. Dann kann eine spektrale Entfaltung in der Time Domain durchgeführt werden zwischen den gemessenen MRSI Daten und den Simulierten Profilen der Resonanzen. odMRSI Rekonstruktion erhöht hauptsächlich das Signal-zu-Rausch (SNR) Verhältnis durch Entkoppelung des spektralen Rauschens zwischen den Subspektren während des Interpolationsschrittes. SPREAD erhöht die spektrale Auflösung durch Reduktion der spektralen Linienbreite, welche durch B_0 Inhomogenitäten verursacht wird.

Beide Methoden wurden zuerst in Simulationen validiert und dann auf Phantom und in vivo Daten angewendet. Eine wesentliche Verbesserung der spektralen Qualität wäre deshalb ein wertvoller Teil der bereits etablierten Nachbearbeitungspipeline. Letztendlich, kann ein höheres SNR in eine Reduktion der Messzeit, höhere spektrale Auflösung oder für eine zuverlässigere Detektierung von niedrig konzentrierten Metaboliten umgewandelt werden.

Unsere Ergebnisse validieren frühere Ergebnisse die eine Verbesserung der spektralen Eigenschaften (höheres SNR) durch odMRSI beobachtet haben. odMRSI Rekonstruktion war robust gegen Einflüsse durch niedriges SNR und kann ebenso auf Frequenzshiftmaps, welche aus den MRSI Daten selbst gewonnen werden, basieren. Das heisst, dass odMRSI ohne zusätzliche Messzeit angewendet werden kann. Allerdings konnte diese Verbesserung in der spektralen Qualität nicht in bessere Metabolitenkarten, welche durch spektrale

Quantifizierung gewonnen werden, umgewandelt werden. Stattdessen lässt dies darauf schliessen, dass die Verbesserung der spektralen Eigenschaften lediglich „kosmetisch“ sind. Im Gegensatz dazu war SPREAD in der Lage die spektralen Eigenschaften nur dann zu verbessern, wenn bereits ein hohes SNR vorhanden war, was in der klinischen Realität kaum der Fall ist.

Basierend darauf können wir rückschliessen, dass sowohl SPREAD als auch odMRSI Rekonstruktion nicht in der Lage sind in einem (klinischen) In vivo Setting Metabolitenkarten von höherer Qualität zu liefern.

Acknowledgements

On this place, I would like to thank Wolfgang Bogner for giving me the opportunity to work at the MR center and for supervising my master thesis. Furthermore, I would like to thank Karin Poljanc and Gerald Badurek for supervising my thesis at the Vienna University of Technology.

Last but not least I would like to thank all my colleagues at the MR center for all discussions, related and unrelated to the topic of the thesis.

Contents

Declaration of Authorship	iii
Abstract	vi
Acknowledgements	ix
1 Introduction	1
1.1 NMR basics	1
1.1.1 Nuclear Zeeman Splitting	1
1.1.2 Spin precession	2
1.1.3 Spin-Lattice Relaxation - Magnetization of Tissue	3
1.1.4 Transverse Relaxation - Signal Detection	4
1.2 NMR Spectroscopy	6
1.2.1 Chemical Shift	6
1.2.2 Fourier Transform of FID	6
1.2.3 Time-domain Filtering	7
Exponential weighting	8
Lorentz-Gaussian transformation	8
1.2.4 Signal Averaging	8
1.3 Magnetic Resonance Imaging	9
1.3.1 Magnetic Field Gradients	9
1.3.2 Slice selection	10
1.3.3 Frequency encoding	10
1.3.4 Phase encoding	12
1.3.5 Spatial Frequency Space - kSpace	13
1.3.6 Magnetic Resonance Spectroscopy Imaging	14
Spatial Resolution in MRSI	15
Spatial Filtering	16
1.4 Main Magnetic Field	16
1.4.1 Inhomogeneity of Main Magnetic Field	17
1.4.2 Correction of Magnetic Field Inhomogeneity	18
1.4.3 Magnetic Field Mapping	20

1.5	Post-processing methods based on high resolution B0 maps . . .	21
1.5.1	Overdiscrete MRSI reconstruction	21
1.5.2	Spectral Resolution Amelioration by Deconvolution . . .	22
2	Materials and Methods	25
2.1	Implementation of odMRSI	25
2.2	Implementation of SPREAD	26
2.3	Simulations	26
2.3.1	Simulation model	26
2.3.2	Simulation of MRSI acquisition	27
2.3.3	Validation of odMRSI on simulated data	28
2.3.4	Validation of SPREAD on simulated data	30
2.3.5	Statistical analysis of the results from the simulations .	31
2.4	Phantom Validations	31
2.4.1	Phantom Validation of odMRSI	32
	Statistical analysis	33
2.4.2	Phantom Validation of SPREAD	33
2.5	In vivo Validation	35
2.5.1	Data acquisition	35
2.5.2	Data Processing	35
2.5.3	Statistical analysis	36
3	Results	39
3.1	Results of Simulations	39
3.1.1	Simulation results for odMRSI	39
3.1.2	Simulation results for SPREAD	42
3.2	The results of Phantom Validation of odMRSI	46
3.3	The results of inVivo validation	50
3.4	The result of validation of odMRSI against signal averaging .	57
4	Discussion	65
4.1	Validation of methods on the simulated data	66
4.2	Validation of methods on the phantom data	66
4.3	Validation of methods on the in vivo data	67
4.4	Limitations and Outlook	67
5	Conclusion	69
	Bibliography	71

List of Figures

1.1	NMR splitting	2
1.2	Spin Polarization Axis without Magnetic Field	3
1.3	Spin Polarization Axis in Magnetic Field	4
1.4	Fourier transformation of FID signal	7
1.5	Slice selection	11
1.6	2D Fourier transform of kSpace	12
1.7	Filling the kSpace	13
1.8	Scheme of the phase encoding MRSI	14
1.9	Example of B0 map	20
1.10	Subvoxel spectra of a MRSI voxel	21
1.11	The postprocessing frequency shift of subvoxel spectra	22
2.1	B0 map for simulation model	27
2.2	Simulation model for validation odMRSI and SPREAD	28
2.3	Simulation model after simulated MRSI acquisition	29
2.4	Parameters for the Hankel Lanczos Squares Singular Values Decomposition.	34
2.5	Example of the MRSI spectra after SPREAD	34
2.6	The pipeline of post-processing of the in vivo MRSI data.	36
2.7	Randomly sampled mask for statistical analysis	37
3.1	Boxplots of the SNR increase for the odMRSI simulation.	40
3.2	Maps of the SNR increase for the odMRSI simulation.	40
3.3	Boxplots of the FWHM increase for the odMRSI simulation.	41
3.4	Maps of the FWHM increase for the odMRSI simulation.	41
3.5	Plot of the standard deviation of subvoxel against the increase of the SNR after odMRSI	42
3.6	Boxplots of the SNR increase for the SPREAD simulation.	43
3.7	Maps of the SNR increase for the SPREAD simulation.	43
3.8	Boxplots of the FWHM increase for the SPREAD simulation.	44
3.9	Maps of the FWHM increase for the SPREAD simulation.	44
3.10	Boxplots of the SNR for the phantom validation of the odMRSI.	48

3.11	Boxplots of the FWHM for the phantom validation of the odMRSI.	48
3.12	Boxplots of the CRLBs of the fitted metabolites for phantom validation of odMRSI, performed on the 16×16 resolution MRSI data.	49
3.13	Boxplots of the CRLBs of the fitted metabolites for phantom validation of odMRSI, performed on the 32×32 resolution MRSI data.	49
3.14	Boxplots of the SNR from the in vivo validation of the odMRSI	53
3.15	Boxplots of the FWHM from the in vivo validation of the odMRSI	54
3.16	Boxplots of the CRLBs of the fitted metabolites for in vivo validation of odMRSI, performed on the 64×64 resolution MRSI data.	55
3.17	Boxplots of the CRLBs of the fitted metabolites for in vivo validation of odMRSI, performed on the 100×100 resolution MRSI data.	56
3.18	Boxplots of the SNR from the comparison of the odMRSI against the Signal averaging.	60
3.19	Boxplots of the FWHM from the comparison of the odMRSI against the Signal averaging.	61
3.20	Boxplots of the CRLBs of the fitted metabolites for comparison of the odMRSI against the Signal averaging.	62
3.21	Comparison of metabolic maps of the Glu+Gln between the Signal averaging and the odMRSI reconstruction.	63
3.22	Ratio of the Ins to the NAA+NAAG metabolic map.	64

List of Tables

1.1	Spherical and Cartesian representation of low-order ($n \leq 4$) spherical harmonics functions.	19
2.1	Concentration of metabolites inside the phantom	31
2.2	The composition of the buffer inside the phantom	32
3.1	The data for the statistical analysis of the simulations.	45
3.2	The result of the statistical analysis of the data from the simulations	45
3.3	The results of statistical analysis for phantom validation.	47
3.4	The results of statistical analysis for in vivo validation of odMRSI reconstruction.	51
3.5	The results of statistical analysis for in vivo validation of odMRSI reconstruction.	52
3.6	The results of statistical analysis for comparison of the odMRSI against the Signal averaging on in vivo dataset (4 averages and 5 averages).	58
3.7	The results of statistical analysis for comparison of the odMRSI against the Signal averaging on in vivo dataset (6 averages).	59

List of Abbreviations

NMR	Nuclear Magnetic Resonance
MRI	Magnetic Resonance Imaging
MRS	Magnetic Resonance Spectroscopy
MRSI	Magnetic Resonance Spectroscopy Imaging
T₁	the spin-lattice relaxation constant
T₂	the spin-spin relaxation constant
T₂[*]	the apparent spin-spin relaxation constant
FID	Free Induction Signal
TMS	Tetramethylsilane
FWHM	Full Width at Half Maxima
SNR	Signal to Noise Ratio
CRLBs	Cramer-Rao at Lower Bounds
RMS	Root-mean-square
FFT	Fast Fourier Transform
FOV	Field of view
PSF	Point Spread Function
DSV	Diameter of Spherical Volume
GE	Gradient Echo
odMRSI	Over Discrete MRSI reconstruction
SPREAD	Spectral Resolution Amelioration by Deconvolution
TE	Echo Time
TR	Repetition Time
TM	Mixing Time
SVD	Singular Values Decomposition
HLSVD	Hankel Lanczos Squares Singular Values Decomposition
STEAM	Stimulated Echo Acquisition Mode
MP2RAGE	Magnetization-Prepared Rapid Acquisition Gradient Echo
CAIPIRINHA	Controlled Aliasing in Parallel Imaging Results in Higher Acceleration
MUSICAL	Multichannel Spectroscopic Data Combined by Matching Image Calibration Data

Chapter 1

Introduction

The first chapter describes theoretical background of the concepts used in the thesis. It is focused on the basics of the Nuclear Magnetic Resonance (NMR), the NMR Spectroscopy, Magnetic Resonance Spectroscopy Imaging (MRSI), and the inhomogeneity of the main magnetic field. Last two sections describe two post processing methods to improve the quality of the spectra obtained by the MRSI.

The more detailed introduction can be found in books: "Spin dynamics" by Levitt [1] or "in Vivo NMR Spectroscopy" by de Graff [2].

1.1 NMR basics

The NMR phenomenon depends on the particles with a non-zero spin number. If such particles are placed in the strong magnetic field, they exhibit the Nuclear Zeeman splitting which yields to a magnetization of the sample. The magnetization can be detected and its origin can be inspected.

1.1.1 Nuclear Zeeman Splitting

A particle, which rotates around some fixed point has the angular momentum. In quantum mechanics, the angular momentum L of the particle is quantized and its amplitude is given by equation 1.1

$$L = \left(\frac{h}{2\pi} \right) \sqrt{J(J+1)} \quad (1.1)$$

where J can have only integer values.

The second quantum number M_J specifies direction of rotation and can have integer values $M_J = -J, -J+1, \dots, +J$. Each state with the same J value has the same energy. The degeneracy is broken in the presence of an external magnetic field. This is called Zeeman effect.

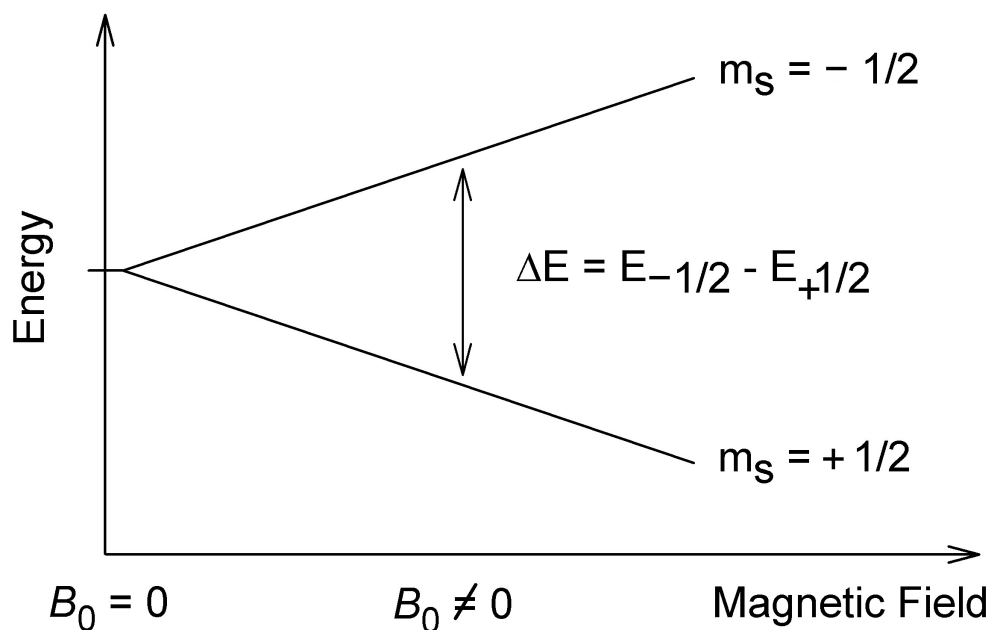


FIGURE 1.1: NMR splitting of a nuclei with $S = 1/2$.

The Spin angular momentum is the form of angular momentum, which is not produced by a rotation but it is an intrinsic property of a particle [1]. A particle with spin S has $(2S + 1)$ degenerate sublevels. The degeneracy is canceled when the particle is placed in a strong magnetic field, which is called Nuclear Zeeman Splitting.

Of major importance in NMR are nuclei with $S = 1/2$. The Nuclear Zeeman Splitting of such nuclei is shown on figure 1.1 (e.g., proton nucleus).

1.1.2 Spin precession

The angular momentum of a particle with spin is a vector, same as the angular momentum of rotating object. The direction of the spin angular momentum is called spin polarization axis and in the absence of an external magnetic field can point in all possible direction. The situation is depicted by figure 1.2. The magnetic moment of a particle has the same direction as the spin polarization axis in case of positive gyromagnetic ratio or opposite in the case of negative gyromagnetic ratio.

If we place a particle into a strong magnetic field, the spin polarization axis starts to rotate around the magnetic field vector. The magnetic moment of the spin moves on a cone, keeping a constant angle between the spin magnetic moment and the field. This motion is called precession. The angle of

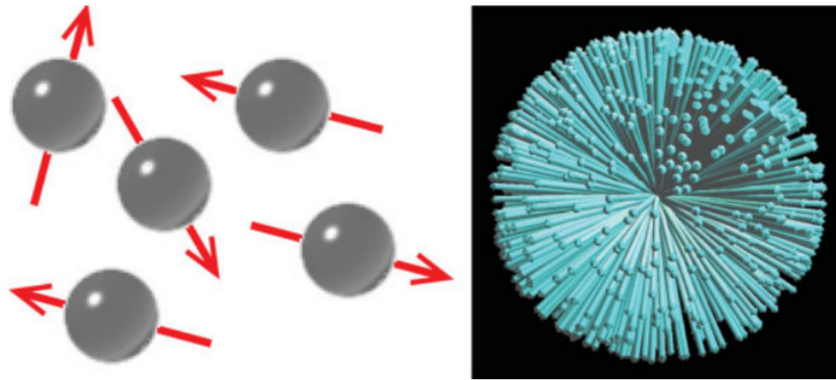


FIGURE 1.2: Left: Different spin polarization axis of particles. Right: A large number of spin polarization axis form spherical distribution.[3]

the cone depends purely on initial spin polarization. The angular frequency of the precession is given by

$$\omega_0 = -\gamma B_0 \quad (1.2)$$

where γ is the gyromagnetic ratio of a particle, B_0 is the external magnetic field and ω_0 is the Larmor frequency.

1.1.3 Spin-Lattice Relaxation - Magnetization of Tissue

If we place a sample of water into the magnetic field an isotropic orientation of spin polarizations of ^1H nuclei do not build net magnetization of the sample immediately.

However, each water molecule experiences, additionally to the external magnetic field, small magnetic fields from its surrounding. This small fields rapidly vary in time because of thermal motion of the environment. Therefore, each spin experiences magnetic field with tiny fluctuations in magnitude and direction, which disturbs the constant angle of precession. The angle of cone precession can wander in all possible direction. The wandering is not completely isotropic because of the finite temperature of an environment. The thermal wandering motion is driven towards spin orientation with magnetization moment parallel to the magnetic field. This yields to an anisotropic distribution of spins polarizations called thermal equilibrium and built net magnetization of the sample, shown on figure 1.3.

The building of net magnetization begins when the sample is brought to a magnetic field or magnetic field is suddenly turned on. The curve of this

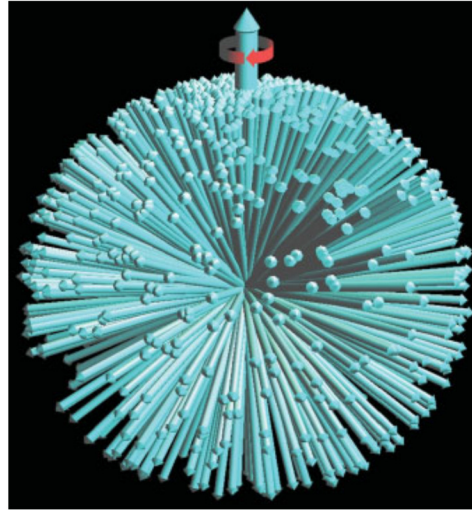


FIGURE 1.3: Anisotropic distribution of a large number of a spin polarization axis in the presence of magnetic field.[3]

effect is usually exponential. If we consider magnetic field in z-direction the curve is given by

$$M_z(t) = M_{eq} \left(1 - e^{-(t-t_{on})/T_1}\right) \quad (1.3)$$

where M_{eq} is magnetization in thermal equilibrium inside the magnetic field, t_{on} is time point in which the sample starts to experience a magnetization field, T_1 is the spin-lattice relaxation constant. The T_1 constant depends on the nuclear isotope and the sample. Typical T_1 values are in the range of milliseconds to seconds for biological tissue.

1.1.4 Transverse Relaxation - Signal Detection

In NMR experiments, instead of longitudinal magnetization, transverse magnetization is measured, which is perpendicular to the main magnetization field. In order to rotate the net magnetization moment of a sample from the z-axis to the xy-plane, we apply the oscillating magnetization field in the direction perpendicular to the main magnetization field with appropriate frequency and duration. This oscillating magnetization field is called RF-pulse.

The net magnetization moment consists of a large number of spins, which precess around the main magnetization field, therefore the transverse magnetization moment also precesses with the same frequency. The transverse magnetic moment slowly decays because of the T_2 relaxation (or spin-spin relaxation), characterized by the T_2 relaxation constant. The T_2 relaxation

is an entropy-process, in which spins exchange the energy between themselves and cause a decrease in phase coherence. However in real experiment, the transverse magnetization decay is describe by the T_2^* relaxation constant, which is defined as

$$\frac{1}{T_2^*} = \frac{1}{T_2} + \frac{1}{T_2'} \quad (1.4)$$

where term $1/T_2' = \gamma \Delta B(\vec{r})$, represents the contribution to the signal decay from the magnetic field inhomogeneity. The components of the magnetic moment after RF-pulse are given by

$$M_y = -M_{eq} \cos(\omega_0 t) e^{-t/T_2^*} \quad (1.5)$$

$$M_x = M_{eq} \sin(\omega_0 t) e^{-t/T_2^*} \quad (1.6)$$

The transverse magnetization moment can be detected by a wire coil in close distance to a sample. The oscillating magnetic field induced the oscillating electric current in the coil. The current is called Free Induction Decay (FID) signal.

The oscillation of FID signal is in the range of many hundreds of megahertz, which is faster than current analogue-to-digital converters (ADC). The solution is to use a quadrature receiver. The quadrature receiver combines the FID signal with the reference signal of frequency ω_{ref} to generate a new signal with relative Larmor frequency, which is in order less than 1 MHz. The relative Larmor frequency is given by

$$\Omega^0 = \omega^0 - \omega^{ref} \quad (1.7)$$

NMR signal has real and imaginary part, which are combined into complex signal given by

$$s_{\text{NMR}}(t) = e^{(i\Omega^0 - 1/T_2)t} \quad (1.8)$$

In addition to the NMR signal the FID signal from quadrupole receiver contains also noise. The noise is a random signal, which has the origin in thermal motions of charged particles in the sample and in thermal motions of electrons in the receiver coil. The FID signal can be seen as

$$s(t) = s_{\text{NMR}}(t) + s_{\text{noise}}(t) \quad (1.9)$$

The ratio between the power of these two parts gives the Signal-to-Noise ratio (SNR), which describe the amount of detected information to the meaningless random signal.

1.2 NMR Spectroscopy

1.2.1 Chemical Shift

According to the equation 1.2 all nuclei of the same element resonate with the same frequency depending on its gyromagnetic ratio and the strength of the external magnetic field. If we take a look at the submolecular distance, the external magnetic field induces currents in the electron clouds in the molecule. The circulating molecular currents generate an induced magnetic field. The magnetic field, which is experienced by the nuclei, is then the sum of the external magnetic field and the induced magnetic field from its environment. This effect is called Chemical Shift and allows to inspect the environment in which the nuclei resonate. The shielding of the nuclei by its environment can be represented by scalar constant σ and the equation 1.2 is modified to

$$\omega_0 = -\gamma B_0 (1 - \sigma) \quad (1.10)$$

Chemical shift is commonly expressed in terms of parts per million (ppm) and it is given by

$$\delta = \frac{\nu - \nu_{ref}}{\nu_{ref}} \times 10^6 \quad (1.11)$$

where ν is the frequency of compound in the sample and ν_{ref} is the frequency of reference compound. As the reference compound, tetramethylsilane (TMS) is usually used because of its independence from external factor as temperature, ionic strength, and shift reagents.

1.2.2 Fourier Transform of FID

The Fourier transform is a mathematical operation, which converts time-domain signal, e.g. given by equation 1.9 into the frequency-domain spectrum. The graphical representation of Fourier transformation is in figure 1.4. The mathematical definition is

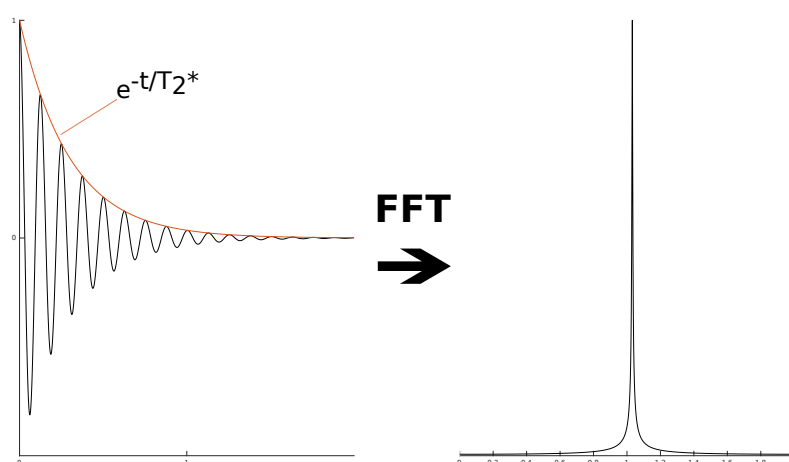


FIGURE 1.4: Left: The real part of the FID signal, decaying by T_2^* relaxation. Right: The magnitude of the spectra.

$$S(\Omega) = \int_0^{\infty} s(t) e^{-i\Omega t} dt \quad (1.12)$$

Both the acquired FID signal and the spectrum of the signal are complex data. The spectrum can be seen as a superposition of complex Lorentzians, where each complex Lorentzian is equivalent to a single oscillating time domain component, in our case chemical compound. The real part of the complex Lorentzian is called absorption Lorentzian, while the imaginary part is called dispersion Lorentzian.

The full-width-at-half-maximum (FWHM) of the absorption Lorentzians is equal to 2λ and $\lambda = T_2^{-1}$. Therefore, fast decaying signals give rise to broad peaks while slow decaying signal result in narrow peaks.

1.2.3 Time-domain Filtering

Time domain filtering allows modifying properties of the spectra, derived from the FID via Fourier transform, by multiplying detected time domain signal by a filter function. The filtering changes the lineshapes of a resonance and also influences SNR and FWHM. Two commonly used filter functions are Exponential weighting and Lorentz-Gaussian transformation.

Exponential weighting

In case that T_w is more than 0, the filter function is decreasing monoexponentially, which is given by

$$f_{\text{filter}}(t) = e^{-t/T_w} \quad (1.13)$$

The filter improves SNR by apodization of the end of the FID, which contains mainly noise. The first part of the FID persists relatively unaffected. However, the resonance FWHM increases because of change in apparent transverse relaxation

$$\frac{1}{T_{2w}} = \frac{1}{T_2^*} + \frac{1}{T_w} \quad (1.14)$$

In case that T_w is less than 0, the filter decreases the SNR but the T_2^* is prolonged, which yields to a lower FWHM and enhancement of spectral resolution.

In general, the sensitivity of detection is traded for spectral resolution. The optimal filter, so-called the Matched filter, is when $T_2^* = T_w$. For this the optimum SNR is achieved by doubling of the FWHM.

Lorentz-Gaussian transformation

The transformation function is given by

$$f_{\text{filter}} = e^{t/T_L} e^{-t^2/T_G^2} \quad (1.15)$$

The function converts the Lorentzian lineshape to Gaussian. In case of the same FWHM, the gaussian lineshape decay faster to the baseline, therefore the transformation enhances the spectral resolution. To achieve significant improvement, a sufficiently long T_G is used, while $T_L = T_2^*$.

1.2.4 Signal Averaging

The FID signal detected by quadruple detector consists of two parts as described by equation 1.9. The first part, which corresponds to the NMR signal is reproducible and can be remeasured if the experiment is repeated. The second part, which corresponds to the noise varies in an irreproducible way. These two different features of measured FID can be used to improve SNR by signal averaging.

If the measurement is repeated n times, the NMR signal is n -fold higher. This rule is not valid for the noise.

The suitable measure of noise amplitude is root-mean-square (RMS) of noise, which is given by

$$\sigma_1 = \langle s_1^2 \rangle^{1/2} \quad (1.16)$$

The RMS of noise from repeated measurement is approximately the same but the noise itself is uncorrelated between different measurements. If we assume two different noise signals, s_1 and s_2 , with approximately the same RMS, $\sigma_1 \approx \sigma_2$, the RMS of summed signal is given by

$$\sigma_{1+2} = \langle (s_1 + s_2)^2 \rangle^{1/2} \quad (1.17)$$

$$= \langle s_1^2 + 2s_1s_2 + s_2^2 \rangle^{1/2} \quad (1.18)$$

$$= \{ \langle s_1^2 \rangle + \langle s_1s_2 \rangle + \langle s_2^2 \rangle \}^{1/2} \quad (1.19)$$

The noise signals are uncorrelated so the term $\langle s_1s_2 \rangle$ vanishes and because the RMS of both signals are approximately equal, equation 1.19 becomes

$$\sigma_{1+2} \approx \sqrt{2}\sigma_1 \quad (1.20)$$

The RMS of summed noise signals from n measurement is \sqrt{n} -fold larger. Finally, if the measurement is repeated n times the SNR therefore increased by the factor of \sqrt{n} .

1.3 Magnetic Resonance Imaging

Magnetic resonance imaging (MRI) provides valuable information about the spatial distribution of nuclei under investigation. The contrast of the final image can be sensitized to different properties of the nuclei such as proton density, T_1 or T_2 relaxation constants.

1.3.1 Magnetic Field Gradients

The Larmor frequency given by equation 1.2 is proportional to the strength of the magnetic field. If an additional linear gradient of the magnetic field strength in one direction is introduced, the Larmor frequency of the nuclei becomes dependent on the position along the gradient. The static magnetic field of an MR scanner is directed along the z-direction and is independent

of the direction of a magnetic gradient. The change is only in the strength of the magnetic field.

The magnetic field gradient is produced in specially shaped coils by electric currents. Usually, three orthogonal gradients are present in the magnetic field. The gradients are arranged in such manner that in the isocenter of the magnetic field their strength is equal to zero.

The strength of the magnetic field with the gradients is given by

$$G(\vec{r}) = B_0 + \vec{r}\vec{G} \quad (1.21)$$

where \vec{r} is a vector of position and \vec{G} is a vector of the strength of magnetic field produced by the gradients. Therefore the equation 1.2 is modified to

$$\omega(\vec{r}) = \gamma(B_0 + \vec{r}\vec{G}) \quad (1.22)$$

This can be used for spatial encoding.

1.3.2 Slice selection

The goal of MRI is to image 3D objects. The encoding position in all three dimension is time-consuming so often the imaging is reduced to several 2D slices. For Slice selection a 2D slice is excited in the presence of a magnetic field gradient by a simultaneously applied RF pulse. Thickness and position of the slice are dependent on the strength of magnetic field gradient and bandwidth of the RF pulse. If the slice selection gradient is in the z-direction, the thickness is given by

$$\Delta z = \frac{\Delta\omega}{\gamma G_z} \quad (1.23)$$

where Δz is the thickness of the slice, $\Delta\omega$ represent the bandwidth of the RF pulse and G_z is the strength of the magnetic field gradient.

According to equation 1.23, a stronger magnetic field gradient yields to thinner slice because the same bandwidth covers less spatial distance, which is depicted in the figure 1.5.

1.3.3 Frequency encoding

If the magnetic field gradient is applied during the data acquisition, the detected signal contains a range of frequencies, which are dependent on the

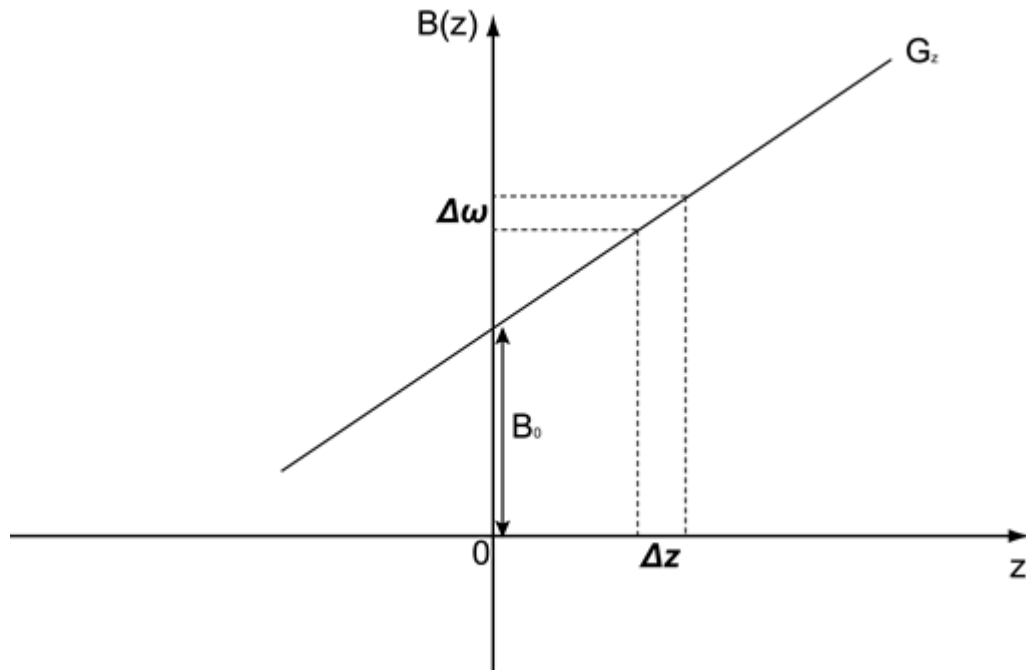


FIGURE 1.5: Relation between thickness of the slice, bandwidth of the RF pulse and the slope of the magnetic field gradient in slice selection [4].

position along the gradient. The Fourier transform of the signal reveals these positions.

Frequency encoding can be applied along any arbitrary direction, which is characteristic for the projection acquisition. The more common way is to use Fourier imaging, where the data are measured into the k-space. The image of the object is then created by spatial Fourier transformation of kSpace.

The frequency encoding gradient typically consists of two lobes, a pre phasing gradient lobe, and a readout gradient lobe applied in the same direction. The pre phasing gradient lobe prepares the transverse magnetization to encode spatial position during the readout gradient lobe.

In a gradient echo sequence, the pre phasing gradient lobe introduce the spatial dependent phase given by

$$\phi_1(\vec{r}) = \gamma \vec{r} \int_0^t \vec{G}(t) \quad (1.24)$$

The readout gradient has opposite sign and it is twice as long as the pre phasing gradient. The total applied gradient moment in the middle of the second lobe is equal to zero and consequently, the acquire phase shift is also equal to zero. The spatial dependent frequencies are given by

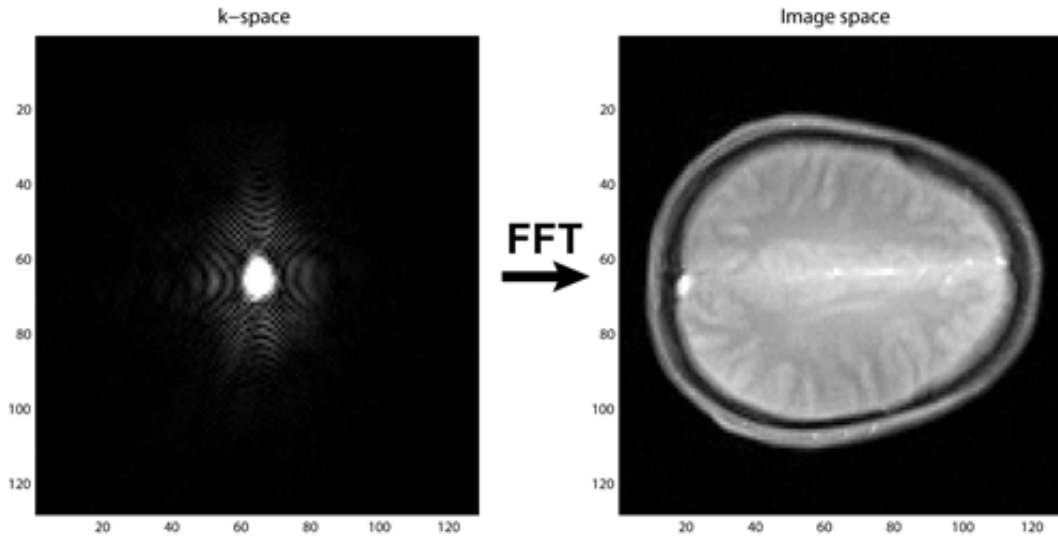


FIGURE 1.6: Transformation of kSpace of an image to image domain [4].

$$\omega(\vec{r}) = \frac{d\phi(\vec{r}, t)}{dt} \quad (1.25)$$

and

$$\phi(\vec{r}, t) = \phi_1(\vec{r}, t_1) + \gamma\vec{r} \int_0^t \vec{G}_2(t) dt \quad (1.26)$$

where t_1 is the length of the first gradient lobe and \vec{G}_2 is the amplitude of the second gradient lobe. Maximum echo formation is when $\phi(\vec{r}) = 0$ for all position \vec{r} , which occurs when $\phi_1(\vec{r}, t_1) = -\phi_2(\vec{r}, t_2)$. Variable t_2 is the half of the duration of the second gradient lobe.

The spatial dependency of frequencies can be clearly seen in equation 1.25.

1.3.4 Phase encoding

In the standard cartesian Fourier imaging, the frequency encoding is performed only in one dimension. The second dimension is encoded by phase. Phase encoding is performed by repetition of the measurement with a gradient magnetic field, gradient of different amplitude is applied, between the excitation and the acquisition of the signal. This results in a variation of the phase between acquired kSpace lines. Finally the image is revealed by performing 2D Fourier transform, which is depicted in figure 1.6.

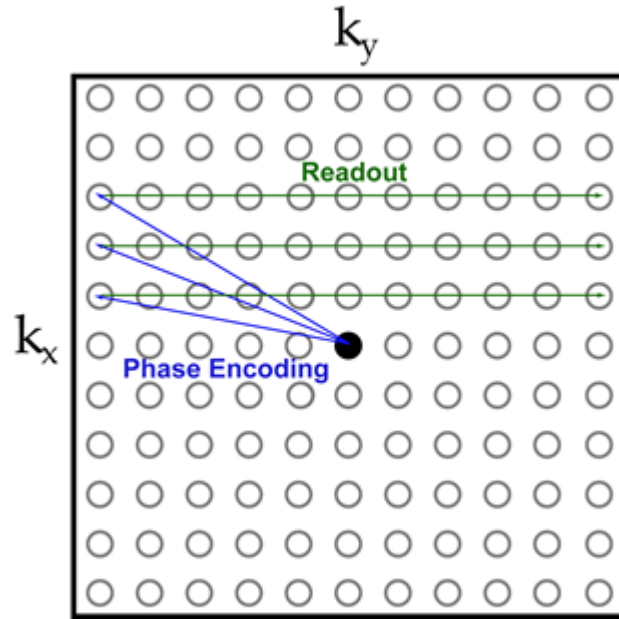


FIGURE 1.7: Filling the kSpace during the measurement, using the phase encoding and frequency encoding gradient [4].

Phase encoding can be solely used for signal localization, e.g. in the Magnetic Resonance Spectroscopic Imaging, but this is very slow.

1.3.5 Spatial Frequency Space - kSpace

In the presence of a time dependent magnetic field gradient $\vec{G}(t)$, the detected signal has the form

$$M_{xy}(\vec{G}, t) = \int_{-\infty}^{\infty} M_0(\vec{r}) e^{i\gamma\vec{r} \int_0^t \vec{G}(t) dt} d\vec{r} \quad (1.27)$$

where $M_0(\vec{r})$ is the proton density at position \vec{r} . By introducing a spatial variable

$$\vec{k}(t) = \gamma \int_0^t \vec{F}(t) dt \quad (1.28)$$

Equation 1.27 becomes

$$M_{xy}(\vec{k}(t)) = \int_{-\infty}^{\infty} M_0(\vec{r}) e^{i\gamma\vec{k}(t)\vec{r}} d\vec{r} \quad (1.29)$$

The process of measuring can be seen as the filling of kSpace with a finite number of $\vec{k}(t)$ values, which is seen in figure 1.7.

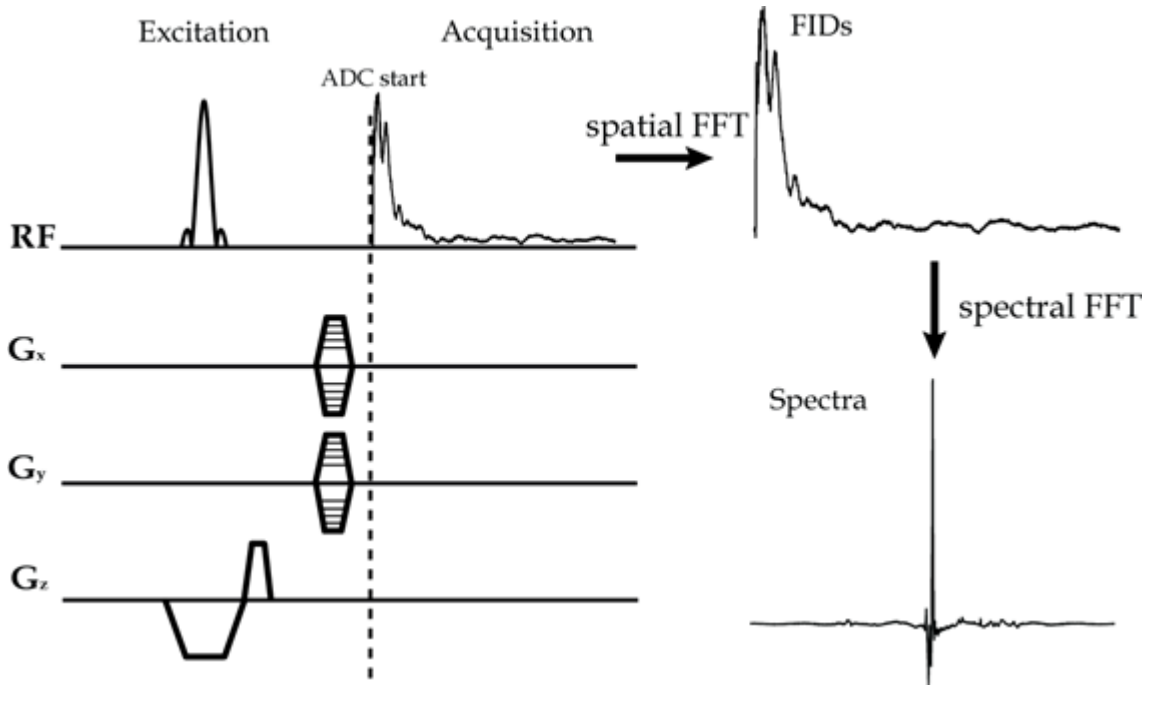


FIGURE 1.8: Spatial localization of FID by phase encoding in both spatial direction. The measured kSpace is transformed to image domain. Each voxel contains FID, which can be transformed to its spectra [4].

1.3.6 Magnetic Resonance Spectroscopy Imaging

The spatial localization for simple phase encoded MRSI is very similar to phase encoding in MRI. After slice selection, the phase encoding is performed in both spatial dimensions and for each kSpace point, several FID time points are measured. Therefore, an additional axis is introduced, in which a time evolution of signal is recorded. The localized spectra can be obtained by the Fourier transform of signal in time dimension, but first the spatial Fourier transform has to be performed. This approach is depicted in figure 1.8

For the one dimension in x-direction, the total acquired time-domain signal is equal to the sum of the signals from elementary volume elements $s(x, t)$ from each point of the sample, which is described by

$$S(t) = \int_{-\infty}^{+\infty} s(x, t) dx \quad (1.30)$$

The total spectrum of the sample $F(\omega)$ is given by the Fourier transform of $S(t)$ and is also equal to the sum of the spectra from each point of the sample $f(x, \omega)$. After the application of phase encoding the phase of spectra is shifted and it can be described by a phase modulation term $e^{i\gamma x G_x t}$. The

spectrum can be written as

$$F(G_x, \omega) = \int_{-\infty}^{+\infty} f(x, \omega) e^{i\gamma x G_x t} dx \quad (1.31)$$

By introduction of kSpace formalism, $k_x = \gamma G_x t$, equation 1.31 can be rewritten to

$$F(k_x, \omega) = \int_{-\infty}^{+\infty} f(x, \omega) e^{ik_x x} dx \quad (1.32)$$

The phase modulated spectra of the entire sample $F(k_x, \omega)$, represents the inverse Fourier transformation of the spectra from the individual points of the sample $f(x, \omega)$. Therefore these spectra can easily be obtained by Fourier transformation of $F(k_x, \omega)$

$$f(x, \omega) = \int_{-\infty}^{+\infty} F(k_x, \omega) e^{ik_x x} dx \quad (1.33)$$

The extension of this calculation to all three spatial dimensions yields

$$f(x, y, z, \omega) = \int_{-\infty}^{+\infty} \int_{-\infty}^{+\infty} \int_{-\infty}^{+\infty} F(k_x, k_y, k_z, \omega) e^{i(k_x x + k_y y + k_z z)} dx dy dz \quad (1.34)$$

In reality, it is impossible to continuously sample kSpace over an infinitely long period so the kSpace is sampled at discrete positions of kSpace over finite time points. Spatially resolved spectra are then obtained by a discrete Fourier transformation.

Spatial Resolution in MRSI

The nominal spatial resolution depends on the FOV and the number of phase gradient encoding increment.

$$\Delta V = \frac{(FOV)}{N_p} \quad (1.35)$$

Due to the Fourier transformation of discretely sampled kSpace, the actual resolution deviates from the equation above and it is defined as the full width at half maxima (FWHM) of the point spread function (PSF). The PSF is described as the Fourier transform of the sampling grid. Effects of the PSF are the increase in actual resolution and the signal leakage. Signal leakage means that the signal from the desired voxel volume is contaminated by signal from the surrounding voxels.

Spatial Filtering

The signal leakage of the PSF can be reduced by spatial apodization, which are applied in the kSpace domain. The apodization functions need to be symmetrical around the origin of the kSpace. The most commonly used functions are the cosine apodization function, the Gaussian function or the Hamming function.

The cosine function is given by

$$W(k) = \cos\left(\frac{\pi k}{2k_{\max}}\right) \text{ for } -k_{\max} \leq k \leq k_{\max} \quad (1.36)$$

where k_{\max} is the maximum sampled position in kSpace. The ripples are significantly reduced but also traded with increased width of the main lobe. The ripples can be reduced even more by the Gaussian function given by

$$W(k) = e^{-4(k/k_{\max})^2} \text{ for } -k_{\max} \leq k \leq k_{\max} \quad (1.37)$$

The reduction of signal bleeding is again traded by an increase of FWHM, thus reducing spatial resolution. The optimal filter is given by the Hamming function,

$$W(k) = 0.54 + 4.46 \cos\left(\frac{\pi k}{k_{\max}}\right) \text{ for } -k_{\max} \leq k \leq k_{\max} \quad (1.38)$$

In all three cases, the FWHM slightly increases. From the time efficiency point of view using the spatial filters is not optimal. The apodization reduces information obtained from high-frequency kSpace coordinates, which measured in same number of averages as the low-frequency coordinates. The solution can be to mimic apodization function by a number of averages for a different position in kSpace during the acquisition (i.e. introducing kSpace weighting during acquisition).

1.4 Main Magnetic Field

Typically the main magnetic field is created by superconducting magnets in almost all modern MR scanners. This type of magnets allows to produce strong magnetic fields up to several Tesla. The superconduction is a property of a superconducting material when the electric resistance is equal to

zero. This condition is fulfilled when the temperature of the material is below its critical temperature. The critical temperature for given material depends on the strength of present magnetic field and the current, which flows through the material. The most common material to produce the magnetic fields in superconducting magnets is niobium titanium alloy (NbTi) with the critical temperature 10K. At the temperature 4.2K, the field up to 10T can be produced. By lowering the temperature to 2.3K, the strength of the magnetic field can be maximized to 12T. To produce even stronger magnetic field the different materials must be used, such as compounds of niobium and tin (Nb_3Sn) or magnesium di-boride.

1.4.1 Inhomogeneity of Main Magnetic Field

The strength of the main magnetic field is not the only important parameter. Another crucial parameter of the main magnetic field is its spatial homogeneity. The homogeneity is given in units of ppm. For MRI the homogeneity of 5 ppm is required and for MRS to clearly distinguish between the choline and total creatine peak a minimum homogeneity is 0.1 -0.2ppm [2]

The field homogeneity is optimized over a diameter of spherical volume (DSV), which is approx. 40-50 % of the whole bore diameter. Theoretically the homogeneity without any manufacturing errors can be less than 1ppm over the DSV, but in practice actual homogeneity of a bare superconducting magnet is typically more than 20 ppm over DSV. The optimization of the homogeneity without sample or patient is usually done during the installation of the MR scanner.

After this, the major origin of inhomogeneities of the main magnetic field is introduced by the sample itself. Variations in the magnetic susceptibility between different tissues types with different magnetic susceptibility lead to disturbance of the main magnetic field. In the human head, the largest differences in the magnetic susceptibility appear at the border between the brain and air in the nasal and auditory passages. The results are strong magnetic field imperfections in the frontal cortex and temporal lobes.

The variation in magnetic field in MRI can cause image distortion and signal loss. In MRSI the inhomogeneities lead to loss of sensitivity and spectral resolution, the misalignment of spectra from different voxels. Moreover the variations inside the MRSI voxel cause the line broadening of spectra.

1.4.2 Correction of Magnetic Field Inhomogeneity

The imperfection of the magnetic field inside the MR scanner can be balance by additional magnetic fields, which consist of the variation described by the spherical harmonics. The sum of these additional magnetic fields can be quantitatively describe by

$$B(x, y, z) = B_0 + \sum_{n=1}^{\infty} \sum_{m=-n}^{+n} C_{n,m} F_{n,m}(x, y, z) \quad (1.39)$$

the functions $F_{n,m}(x, y, z)$ are given in table.

The correction of imperfections in the magnetic field is called B0 field shimming. The additional magnetic fields can be produced by shim coils (electromagnets) or by additional static magnets.

The shimming performed by additional static magnets is called passive shimming. The magnets do not have to be permanent magnets but can be in form of diamagnetic, paramagnetic or ferromagnetic and be magnetized by the main magnetic field, e.g. a small piece of iron. The shimming is performed by optimization of its spatial position. The disadvantage of passive shimming is that the magnetic properties of the materials are temperature dependent, which can lead to field drift and changes in homogeneity during the measurement.

The shim coils can be placed in the bore of the magnet and operate at room temperature. These shim coils are resistive coils and are wound from copper wire or etched from copper sheet. They need a high-stability power supply and in combination with the passive shimming can optimize the field inhomogeneity introduced by the investigated sample.

Shim coils are also located in the helium vessel. These coils are wound by superconducting wire. The current is optimize during the installation of the magnet for correction of the inhomogeneity caused by the manufacturing process.

TABLE 1.1: Spherical and Cartesian representation of low-order ($n \leq 4$) spherical harmonics functions.[5]

Order	Degree	$P(\theta)^a$	$F(x, y, z)^b$	Common name
0	0	1	1	Z0
1	0	$\cos \theta$	z	Z
1	+1/ -1	$\sin \theta$	x/y	X/Y
2	0	$1/2 (3 \cos^2 \theta - 1)$	$z^2 - 1/2R^2$	Z2
2	+1/ -1	$3 \sin \theta \cos \theta$	$3zx/3zy$	ZX/ZY
2	+2/ -2	$3 \sin^2 \theta$	$3(x^2 - y^2)/6xy$	X2Y2
3	0	$1/2 (5 \cos^3 \theta - 3 \cos \theta)$	$z^3 - 3/2zR^2$	Z3
3	+1/ -1	$3/2 \sin \theta (5 \cos^2 \theta - 1)$	$6x(z^2 - 1/4R^2)/6y(z^2 - 1/4R^2)$	Z2X/Z2Y
3	+2/ -2	$15 \sin^2 \theta \cos \theta$	$15z(x^2 - y^2)/30zxy$	ZX2Y2/ZXY
3	+3/ -3	$15 \sin^3 \theta$	$15x(x^2 - 3y^2)/15y(3x^2 - y^2)$	X3/Y3
4	0	$1/8 (35 \cos^4 \theta - 30 \cos^2 \theta + 3)$	$z^4 - 3z^2R^2 + 3/8R^4$	Z4
4	+1/ -1	$5/2 \sin \theta (7 \cos^3 \theta - 3 \cos \theta)$	$10zx(z^2 - 3/4R^2)/10zy(z^2 - 3/4R^2)$	Z3X/Z3Y
4	+2/ -2	$15/2 \sin^2 \theta (7 \cos^2 \theta - 1)$	$45(x^2 - y^2)(z^2 - 1/6R^2)/90xy(z^2 - 1/6R^2)$	Z2C2/Z2S2
4	+3/ -3	$105 \sin^3 \theta \cos \theta$	$105zx(x^2 - 3y^2)/105zy(3x^2 - y^2)$	ZC3/ZS3
4	+4/ -4	$105 \sin^4 \theta$	$105(x^2 - y^2)^2 - 420x^2y^2/420xy(x^2 - y^2)$	X4/Y4

^a only the $P(\theta)$ is given. The complete spherical harmonics function requires multiplication with $r^n \cos(m(\psi - \psi_0))$.

^b $R^2 = x^2 + y^2$

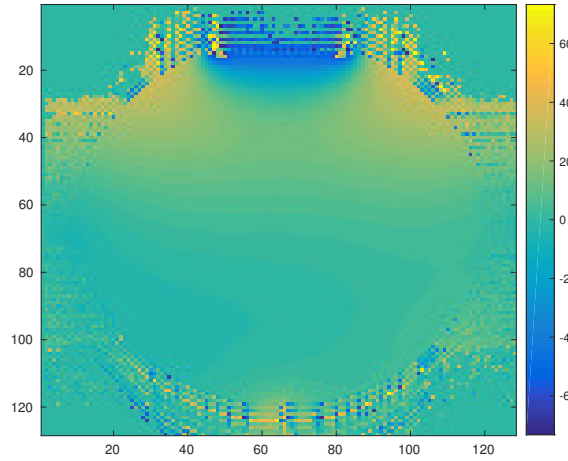


FIGURE 1.9: Example of B_0 map estimated by double spin echo sequence.

1.4.3 Magnetic Field Mapping

The correction of the main magnetic field inhomogeneity is based on its precise measurement. The field mapping of inhomogeneities introduced by patients or samples is usually based on a gradient-echo imaging method, which is fast, easy to use and is inherently sensitive to B_0 offset. Two GE images are acquired with different echo times separated by a constant τ . The phase difference $\Delta\phi$ between two images is directly proportional to the magnetic field distribution

$$\Delta\phi(\vec{r}) = 2\pi\Delta v(\vec{r})\tau \quad (1.40)$$

The location dependent phase difference between the two images is calculated by complex division

$$\Delta\phi = \arctan\left(\frac{R_1I_2 - I_1R_2}{R_1R_2 + I_1I_2}\right) \quad (1.41)$$

where R and I refer to the real and imaginary part of the complex MRI signals acquire at $\tau = 0$ and $\tau > 0$. The additional delay τ is in range of a few *ms*. A sample B_0 map can be found in figure 1.9.

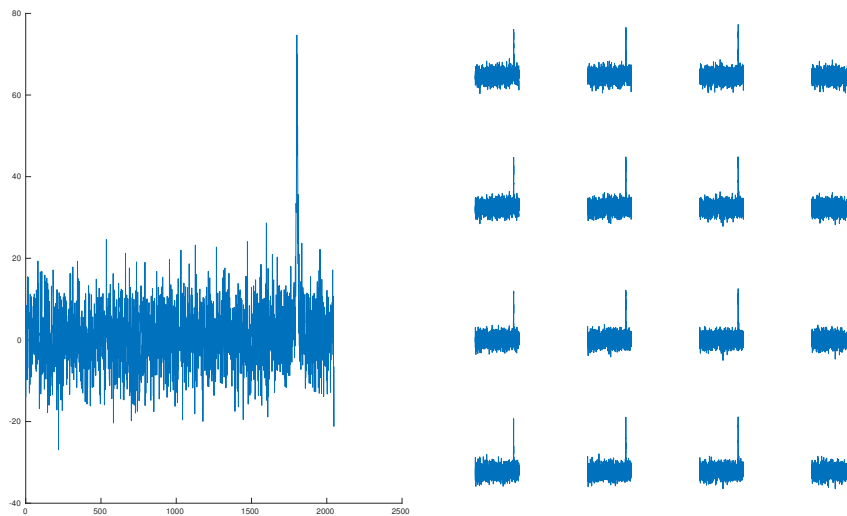


FIGURE 1.10: Left: The spectrum of the MRSI voxel. Right: The subvoxel spectra created by zero-filling interpolation in k Space domain by factor of 4.

1.5 Post-processing methods based on high resolution B_0 maps

Despite the advanced shimming techniques, a certain amount of imperfection in the homogeneity of the main magnetic field still remains. In MRSI, these imperfections cause, besides the effects mentioned above, also the spectral misalignment of the spectra from different voxels. This effect can be corrected by frequency shifting of the spectra during postprocessing. This shifting can be based on a reference peaks inside the spectra or the B_0 map, which sample the continuous nature of the variation just on the grid of the MRSI. However the discrete values of the B_0 inhomogeneities are not able to reflect the intravoxel variation.

1.5.1 Overdiscrete MRSI reconstruction

Overdiscrete MRSI reconstruction (odMRSI), proposed by Kirchner et al.[6], uses the high resolution B_0 map to improve the SNR and spectral line shape. k Space zero-filling is used to interpolate the MRSI to the resolution of the B_0 map. In case of 4-fold larger B_0 map's resolution, the inhomogeneity inside the voxel is represented by 16 subvoxel. After the MRSI interpolation, each subvoxel contains the spectrum, which is depicted in figure 1.10

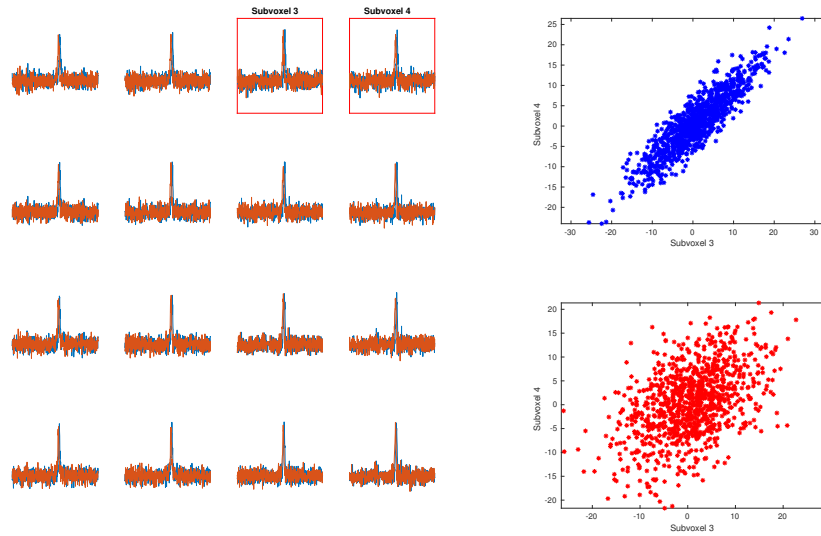


FIGURE 1.11: Left: The real parts of the spectra of the subvoxels. Before (blue) and after (orange) application of the postprocessing frequency shift. Right: The correlation of noise part of the spectra of subvoxel 3 and 4 before (blue) and after (red) the postprocessing frequency shift.

The subvoxel spectra are then alligned by the postprocessing frequency shift. Then the subvoxels inside the main MRSI voxel are averaged together. The alignment of subvoxel spectra has also the side effect of decorrelation of its spectral noise part. This step is depicted in figure 1.11.

Therefore, averaging of the signals with decorrelated noise parts yield higher SNR. Kirchner et al. found an increase of the SNR by factor 3.7 compared to the reconstruction without any filtering and by factor of 3.1 compared to the case of a spatial Hamming filter.

1.5.2 Spectral Resolution Amelioration by Deconvolution

The main goal of the Spectral Resolution Amelioration by Deconvolution (SPREAD) method proposed by Dong and Peterson [7], is to improve spectral resolution of the MRSI by deconvolution of the measured signal with its lineshape profile. The lineshape profile represents the distortions of the spectra, which have the origin in the B0 inhomogeneity.

The method is based on the model of phase encoded MRSI signal given by

$$S(\vec{k}_n, t_d) = \int_{-SW/2}^{SW/2} \int_R \rho(\vec{r}, f) e^{i2\pi(\vec{k}_n + ft_d)} e^{i2\pi\Delta f(\vec{r})t_d} d\vec{r} df \quad (1.42)$$

The measured MRSI signal is given by

$$s_V(t_d) = s_V^0(t_d) \int_V e^{i2\pi\Delta f(\vec{r})t_d} d\vec{r} \quad (1.43)$$

where $s_V^0(t_d)$ is the actual signal, which is being measured, and $e^{i2\pi\Delta f(\vec{r})t_d}$ is the phase term, which represent the distortion from B0 inhomogeneity.

The lineshape profile is then given by

$$L_V(t_d) = e^{i2\pi\Delta f(\vec{r})} \quad (1.44)$$

and the original signal is recover by complex division

$$s_V^0(t_d) = s_V(t_d) / L_V(t_d) \quad (1.45)$$

In the SPREAD method, a high resolution B0 map is obtained and the frequency offsets are computed in similiar way as mentioned above. The frequency offsets are used to simulate the linebroadening and lineshape distortions by equation 1.44. The spatial resolution of the lineshape profile's dataset is as high as the resolution of the B0 map. To lower its resolution, the simulation of real world MRSI acqusition is performed. The measured MRSI signals can then be divided by the lineshape profiles, which is described by equation 1.45. The result should be undistorted an MRSI dataset.

Moreover Dong and Peterson recommend a few post processing steps before the deconvolution. The first is the spatial filtering with a Hamming filter. The next recommendation is to remove the water residua from the spectra. Finally, because of the presence of noise in MRSI data they recommend to use a Wiener-Gaussian filter to suppress the spike artifacts and reduce the noise amplification of their method.

The Wiener-Gaussian filter is given by

$$w(t_d) = G(t_d) \frac{|L_V(t_d)|^2}{|L_V(t_d)|^2 + \alpha K_V(t_d)} \quad (1.46)$$

where G is the Gaussian function, α is a scaling constant, and K_V is defined as

$$K_V(t_d) = \frac{\sigma^2}{|s_V(t_d)|^2} \quad (1.47)$$

while the σ^2 is the noise power, calculated as

$$\sigma^2 = \sum_{\delta} |s_V(t_{\delta})|^2 \quad (1.48)$$

where t_δ is the last part of the signal which contains just noise.

The scaling constant α is calculated as

$$\alpha = L_{V,\max}/s_{V,\max} \quad (1.49)$$

Due to the Wiener-Gaussian filtering the equation 1.45 is modified to

$$s_V^0(t_d) = s_V(t_d) w(t_d) / L_V(t_d) \quad (1.50)$$

Chapter 2

Materials and Methods

This chapter describes the implementation and validation of MRSI methods used for the improvement of spectral quality. The implementation of post processing method was written in MATLAB [8]. The methods were initially tested on a simulation model, written also in MATLAB [8] and validated on phantom data and in vivo data. The spectral quantification of measured data was performed by LCModel [9]. The statistical analysis was again performed in MATLAB [8].

2.1 Implementation of odMRSI

Overdiscrete MRSI reconstruction was implemented in function *overdisceteMR-SIrecon.m*. As input the function needed an MRSI dataset, a high-resolution B0 map and a time vector, which specified the time points at which FIDs had been sampled. The output of the function was a corrected MRSI dataset with the same spatial and time resolution as the input dataset.

The function first estimated the factor between the spatial resolution of the MRSI dataset and the B0 map. In case that the factor between the resolutions was not an integer, the B0 map was interpolated to the closest integer factor of the MRSI resolution. The input MRSI dataset was transformed into the spatial kSpace domain, spatially zero-filled into the high resolution of the B0 map and then transformed back into the iSpace. The result was a high-resolution MRSI dataset with same spatial resolution as the B0 map. The next step was the alignment of the spectra based on the B0 map. Frequency shifting was performed by

$$s_{\text{corr}}(\vec{r}, t) = s_{\text{mes}}(\vec{r}, t) e^{-2\pi i \Delta\nu(\vec{r})t} \quad (2.1)$$

where $s_{\text{mes}}(\vec{r}, t)$ was measured/interpolated FID signal, term $\Delta\nu(\vec{r})$ represents frequency offset caused by the B0 inhomogeneities and t was a time vector.

Finally, the subvoxel's FID signals of the corrected MRSI dataset, which belong to the same low-resolution MRSI voxel, were averaged in the iSpace domain.

2.2 Implementation of SPREAD

Spectral amelioration by deconvolution was implemented in function *SPREAD.m*. As inputs, the function needs a MRSI dataset, a high-resolution B0 map, a time vector, which specified the time points at which FIDs had been sampled and a filter function. The filter function was a decay function with the Gaussian shape and was given by

$$g = e^{\frac{-t^2}{2\sigma^2}} \quad (2.2)$$

where t was a time vector corresponding to the same time points as the FID signal. The σ was the standard deviation of the Gaussian distribution which influenced the width of the gaussian window. The output of the function was the corrected MRSI dataset.

The function first estimated the lineshape profiles based on the high-resolution B0 map according to equation 1.44. The lineshape profile dataset had the same resolution as the B0 map and the same number of time points as the FID. The simulation of the MRSI acquisition was performed in the kSpace domain. The kSpace of the Lineshape dataset was cut to match the spatial resolution of the input MRSI dataset. Then, the spatial Hamming filter was applied and the lineshape profile dataset was transferred to the iSpace domain. The Gaussian-Wiener filter was estimated according to equation 1.46 and finally the deconvolution was performed.

2.3 Simulations

2.3.1 Simulation model

A simulation model was thought as a MRSI slice with a square object in the middle. The matrix size of the slice was 128×128 while the size of the object was 64×64 and was centered in the middle of the slice. The B0 map of

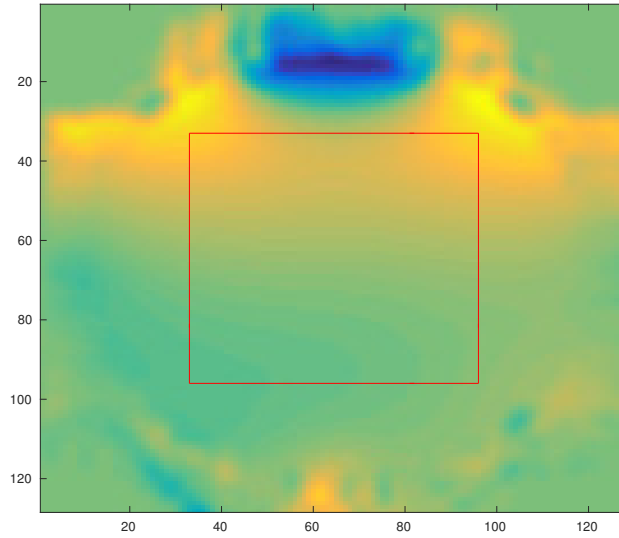


FIGURE 2.1: B0 map for the simulation model. The red square defined the region used for the MRSI simulation.

size 128×128 was used from a phantom measurement, which is specified in section 2.4. Before the MRSI simulation, the B0 map had been smoothed to remove noise variations by a Gaussian filter with standard deviation $\sigma = 2$. The smoothed B0 map is depicted in figure 2.1. To create the model for the MRSI simulation, each voxel, which belongs to the object contained FID signal defined as

$$h_{\text{sim}}(\vec{r}, t) = a_1 e^{2\pi i(\nu_1 + \Delta v(\vec{r})t)} e^{-t/T_2} \quad (2.3)$$

The amplitude was $a_1 = 1$, the frequency was $f_1 = 1500$ Hz and the acquisition duration was 512 ms sampled by 2048 time points. The term $\Delta v(\vec{r})$ represented the magnetic field inhomogeneity in units of hertz. The simulation model is depicted in figure 2.2

2.3.2 Simulation of MRSI acquisition

The MRSI acquisition was simulated in the kSpace domain by cutting the kSpace of the simulation model to low MRSI resolution of size 32×32 . Then a noise matrix was added to the kSpace dataset with the spatial size of 32×32 and 2048 time points. The noise matrix was generated by MatLab's *randn.m* function. Because the FID signal consists of complex numbers, two matrices with zero mean and non-zero standard deviation were used to represent the

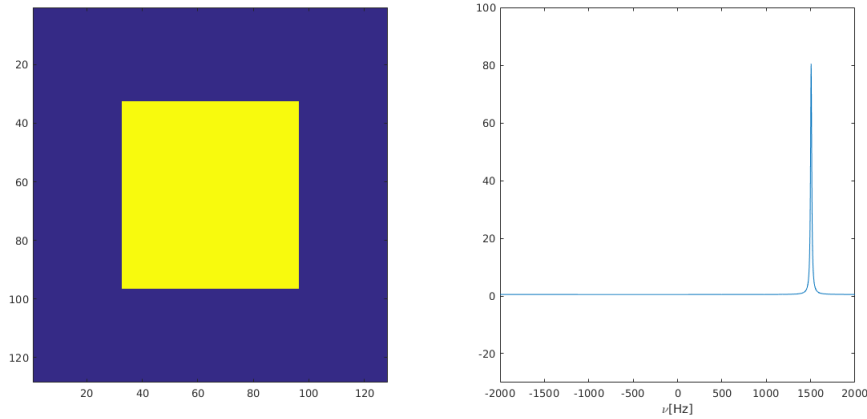


FIGURE 2.2: Left: The image of the first FID point of the simulated MRSI slice. Right: The spectrum of each voxel of the object in the MRSI simulation.

imaginary and the real part of the FID. The standard deviation of the noise matrices was modified to match the desired SNR. After transition back to the *i*Space domain, the MRSI dataset was in size 32×32 and 2048 time points, so the spatial resolution decrease by factor of 4. However the voxel size increase by the same factor and the spectrum of each voxel was influence by the B_0 inhomogeneities from the 4×4 larger space. The situation after the simulated MRSI acquisition is depicted in figure 2.3.

The B_0 map acquisition was simulated by adding noise to the smoothed B_0 map used in the simulation. The standard deviation of simulated noise matrix was estimated as the standard deviation of the difference between the measured B_0 map and its smoothed version from the region where MRSI slice was simulated.

2.3.3 Validation of odMRSI on simulated data

The odMRSI was expected to improve the spectral quality. The spectral quality was represented by the SNR and the FWHM of the spectra. For estimation of both parameters, the two Matlab's function, *SNR_est.m* and *FWHM_est.m*, were written.

The spectral quality, mainly in terms of the SNR, can be also enhanced by investing more acquisition time in form of signal averaging, which is described in section 1.2.4. This method does not influence the FWHM. Therefore in the validation of odMRSI, the average of four measurements was used for comparison. In theory, N averages should bring the SNR improvement

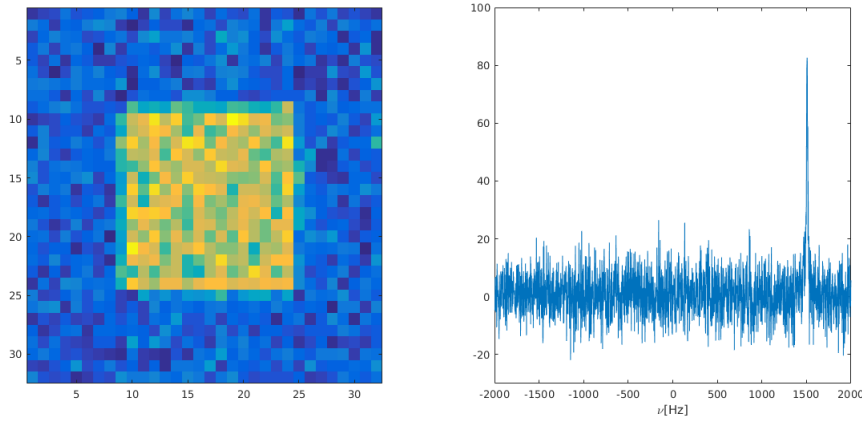


FIGURE 2.3: Left: The image of the first FID point of the simulated MRSI slice. Right: The spectrum of a voxel from the middle of the object.

around factor of \sqrt{N} , so in our case the SNR improvement should be around factor of 2. In the simulation, the repetition of measurement was simulated by generating a new noise matrix.

For validation of odMRSI 5 dataset were used:

- **csi_LD_1mes** - one measurement, which was used as input
- **csi_LD_4mes** - average of four measurement
- **csi_LD_1me_odMRSI_N** - one measurement corrected by odMRSI with a measured B0 map
- **csi_LD_1me_odMRSI_R** - one measurement corrected by odMRSI with a random B0 map
- **csi_LD_1me_odMRSI_S** - one measurement corrected by odMRSI with a modified B0 map

The validation was performed only in the voxels which belong to the simulated object. The maps of the SNR and the FWHM were estimated for all five datasets. The dataset **csi_LD_1mes** was used as a reference, so the improvement in the SNR and the FWHM were represented as a ratio between an improved dataset and an input dataset instead of using absolute values. In case of the SNR, the ratios were estimated as SNR of the improved dataset divided by the SNR of the reference dataset. The ratios of the FWHM were estimated in the same way as for the SNR. The ratio maps of the improvement for the SNR and the FWHM were plotted to inspect spatial dependencies.

Basic statistical properties of the ratios were presented in form of boxplots and compared to the case with 4 simulated measurements.

Because of the additional information, which should improve the spectral properties, using high-resolution B0 maps, the statistical parameters of intravoxel B0 inhomogeneities, mean and standard deviation, were estimated for each MRSI voxel. Maps of means and standard deviations were then correlated with the factor of improvement.

However, the standard deviation of subvoxel inhomogeneities and their mean value can be correlated themselves. Therefore, to reveal the causality of improvement, a modified B0 map was applied in odMRSI, which should represent only the deviation between subvoxel. The modified B0 map was a subtraction between the "measured" B0 map and the mean values of B0 inhomogeneities between intravoxel values.

To prove that the improvement in the odMRSI comes from the intravoxel deviation of B0 map, a random B0 map was applied with zero mean and standard deviation equal to 0.8 Hz.

2.3.4 Validation of SPREAD on simulated data

The SPREAD method reduces the FWHM by deconvolution between the measured FID signal and the biased signal, which has the origin in the intravoxel B0 inhomogeneities. Based on the post processing recommendation mentioned in section 1.5.2, for the validation of SPREAD method four datasets were used:

- **csi_LD_1mes** - one measurement, which was used as input
- **csi_LD_4mes** - average of four measurement, which was used as reference
- **csi_LD_1me_SPREAD** - one measurement corrected by SPREAD
- **csi_LD_1me_GWfilter** - one measurement corrected by Wiener-Gaussian filter

In the same way as in the validation of the odMRSI, the SNR and the FWHM improvement were determined via ratios and plotted as ratio maps to inspect the spatial dependency. The basic statistical parameters were presented in form of boxplot. Also for the comparison, the signal averaging of four measurements was used. The dataset filtered by the Wiener-Gaussian window represented the improvement by the time domain filter and the state

directly before the deconvolution. The standard deviation for the Gaussian filter was 0.5 sec.

2.3.5 Statistical analysis of the results from the simulations

Statistical analysis was performed to find out if the odMRSI and the SPREAD improve the spectral quality. For comparison two cases, before and after applying a post processing method, a paired test is suitable. In case of the normality of differences between paired data, the paired t-test was used. If the condition of the normality was not fulfilled the Wilcoxon signed-rank test was used. The normality was tested by the Anderson-Darling test. All statistical tests were carried out on the 5 % level of significance.

2.4 Phantom Validations

Phantom validation was performed on the 3T whole body MR scanner (Prisma-fit, Siemens Healthcare, Erlangen, Germany) with a 32 channel head coil. The spherical phantom was used which contains common brain metabolites: N-Acetyl-Aspartate (NAA), Choline (Cho), Kreatin (Cr), Glutamine(Gln) and Laktat (Lac) and a buffer. The metabolite concentrations are stated in table 2.1 and composition of the buffer is stated in table 2.2.

The phantom was scanned by a Stimulated Echo Acquisition Mode (STEAM) MRSI sequence with parameters: echo time (TE) 20 ms, mixing time (TM) 10 ms, flip angle 90 degrees, repetition time 1.97 s, field-of-view (FOV) 200×200 mm, slice thickness 10 mm, bandwidth 1200 Hz, vector size 2048. Two matrix sizes, $16 \times 16 \times 1$ and $32 \times 32 \times 1$, were scanned. B0 maps were obtained via double echo gradient echo sequence with parameters: FOV 200×200 mm,

TABLE 2.1: The concentration of metabolites of metabolites used in the phantom.

Metabolit	Molar Mass [g/Mol]	Concentration	
		[mM/l]	[g/l]
NAA	175.1	15.0	2.63
Cr	131.1	10.0	1.31
Cho	139.6	3.0	0.42
Lac	96.0	5.0	0.48
Gln	146.2	12.5	1.83

TABLE 2.2: The composition of the buffer inside the phantom and concentration of used compound.

Compound	Molar Mass [g/Mol]	Concentration	
		[mM/l]	[g/l]
$K_2HPO_2 \cdot 3H_2O$	228.2	72	16.43
KH_2PO_4	136.1	28	3.81
KH_2	68.0	200	13.60

slice thickness 10 mm, TEs were 4.92 and 7.38 ms, flip angle 10 degree and TR 15 ms. Two different matrix sizes 64×64 and 128×128 were scanned.

For validation of odMRSI and SPREAD, the resolution of B0 maps were 4 and 8 fold higher compared to the MRSI dataset of matrix size 16×16 and 2 and 4 fold higher for the case with 32×32 matrix size.

2.4.1 Phantom Validation of odMRSI

The post processing of the data was performed with in-house-developed software, written in Matlab, Bash and MINC [10] and extended by the odMRSI algorithm. Coil combination of MRSI datasets was performed on the scanner using the Brown method [11]. The MRSI data were first filtered by spatial Hamming filter and odMRSI was applied. The corrected datasets were fit by LCmodel. The quality of fitting was represented by Cramer-Rao lower bounds (CRLBs) for each metabolite from a basis set. The output of LCModel was converted to metabolic maps and maps of spectra quality parameters, such as SNR, FWHM, and CRLBs of metabolites.

However, the SNR estimation of LCModel for large SNR values is biased by fitting residua, so the SNR was computed in Matlab by function *SNR_phantom_est.m*. The function estimates the SNR as the ratio between the amplitude of the NAA peak in the magnitude spectrum to the standard deviation of noise in the real spectrum. The magnitude version of the spectrum is used with the assumption that the amplitude of a peak in the magnitude mode is the same as the amplitude of the peak in the real mode of the perfectly phased spectrum, but does not require phasing. The standard deviation was estimated from the part of the spectrum where no signal was visible.

Statistical analysis

Statistical tests were used to test the hypothesis that the odMRSI improves the quality of LCModel fitting. The comparison of the CRLBs of fitted metabolites and spectral quality properties, the SNR and the FWHM, was performed. Based on the used basis set for the fitting, LCModel fitted all metabolites from table 2.1, except the lactate. For the statistical analysis only randomly selected voxels were chosen. The comparison of two cases, before and after applying the odMRSI, suggested using a paired test. Depending on the normality of the difference between these two cases the Student t-test or the Wilcoxon signed-rank test was used. All statistical tests were performed on the 5 % statistical level of significance.

2.4.2 Phantom Validation of SPREAD

The MRSI datasets were the first spatially filtered by the Hamming filter. Dong and Peterson [7] recommend to remove water residua from the spectra, so it was the next step, which was done in JMRUI by The Hankel Lanczos Squares Singular Values Decomposition (HLSVD) [12]. The parameters for HLSVD were: 25 components, 2048 rows in Hankel matrix, 4096 points in SVD and 4096 points to correct. The spectral region of water residue was defined by hand, which is shown on the figure 2.4.

The datasets were loaded to Matlab and the SPREAD method was applied. Each MRSI dataset was corrected with two different B0 maps. The results were compared and evaluated only qualitatively, because the poor performance of the method was immediately apparent. The example of the spectra from phantom dataset corrected by SPREAD method is shown in figure 2.5.

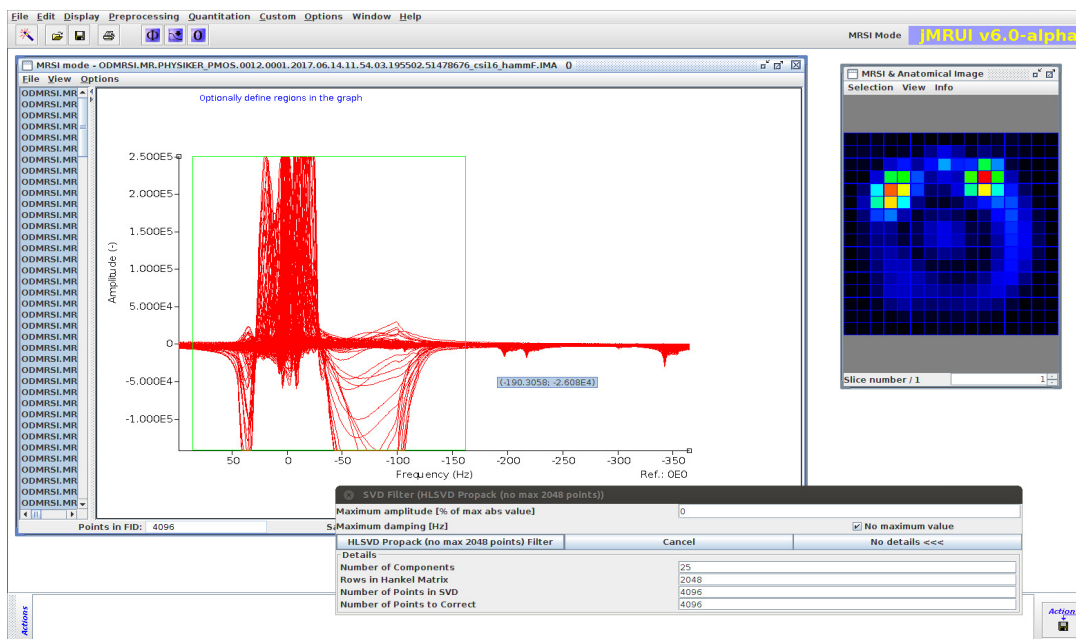


FIGURE 2.4: Definition of parameters for HLSVD with defined region of water residue in JMRUI.

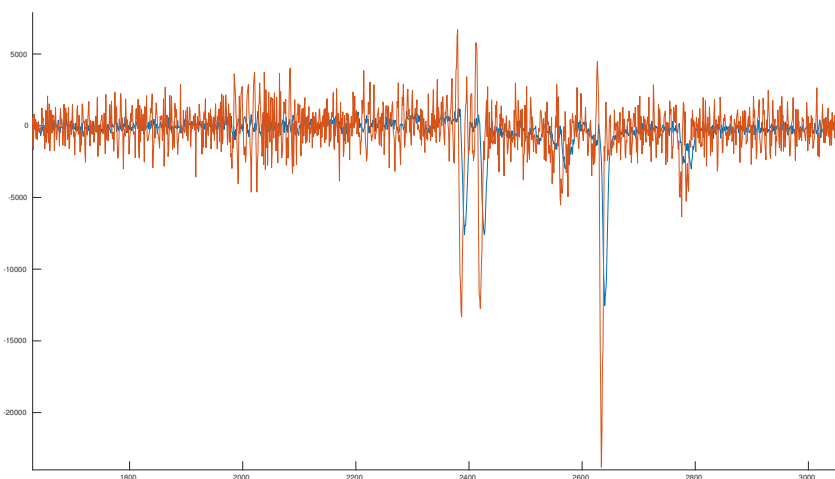


FIGURE 2.5: The MRSI spectra of one voxel before (blue) and after (orange) SPREAD.

2.5 In vivo Validation

Based on the results from the simulations and the phantom validation, only the odMRSI was tested on in vivo datasets. Six healthy volunteers were scanned on a 7T whole body MR scanner (Magnetom, Siemens Healthcare, Erlangen, Germany) with a 32-channel receive coil array combined with a volume transmit coil (NovaMedical, Wilmington, Massachusetts, USA).

2.5.1 Data acquisition

For localization purposes a 3D T_1 -weighted, magnetization-prepared, rapid acquisition gradient echo sequence (MP2RAGE) was acquired [13]. To adjust the intended flip angle a B_1^+ map was acquired with a presaturation turboFLASH-based B_1 mapping sequence [14].

MRSI datasets were acquired with a two-dimensional, FID-based MRSI sequence [15]. For the first five volunteers, two different matrix sizes, 64×64 and 100×100 were acquired, while the other parameters were: FOV, 220×220 mm; slice thickness, 8 mm; TE, 1.3 ms; TR, 450 ms; flip angle, 42° ; vector size, 2048 oversampled FID points; bandwidth, 6000 Hz; elliptical phase encoding. For matrix size 64×64 CAIPIRINHA parallel imaging [16] with acceleration factor $R = 9$ was used, acquisition time was 6 : 26 min. For matrix size 100×100 CAIPIRINHA parallel imaging [16] with acceleration factor $R = 4$ was used and acquisition time was 2 : 38 min. For volunteer number six, six averages of MRSI data of matrix size 100×100 were acquired to compare improvements in spectral quality obtained by odMRSI against the improvement achieved by averaging.

B_0 maps were obtained via the double echo gradient echo sequence with three different matrix sizes, 200×200 , 300×300 , 400×400 . The others parameters: FOV, 220×220 ; slice thickness, 10 mm; TR, 34 ms; TEs, 5.10 and 6.12 ms; flip angle 20°

2.5.2 Data Processing

MRSI data processing was performed offline with an in-house-developed tool [10] based on Matlab, Bash, and MINC, which was extended by the odMRSI algorithm, written in Matlab. Processing pipeline is depicted in figure 2.6. Multichannel spectroscopic data combined by matching image calibration data (MUSICAL) coil combination [17], CAIPIRINHA reconstruction [16] and spatial Hamming filter were applied. Lipid contamination of the

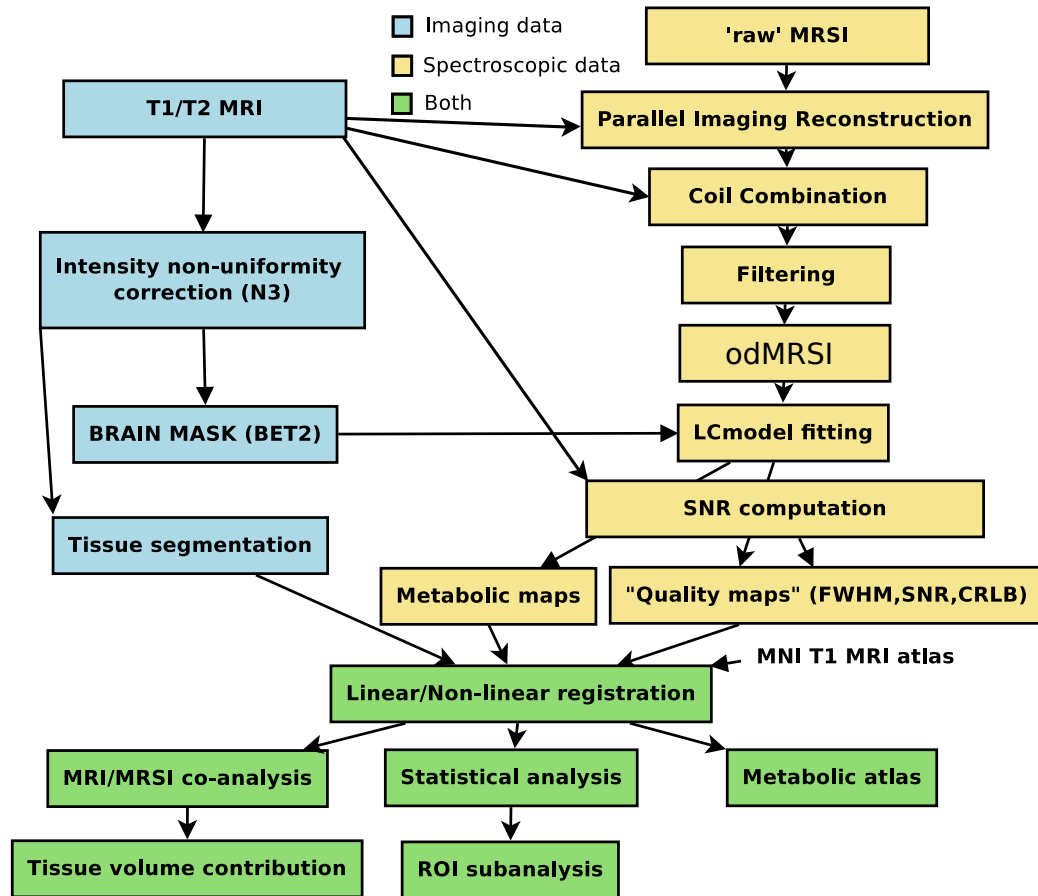


FIGURE 2.6: The pipeline of post-processing of the in vivo MRSI data. [10]

spectra was removed by L2-regularisation [18] and the odMRSI was applied with a high-resolution B0 map. The spectral fitting was performed voxel-wise by LCModel in the range between 1.8 ppm and 4.2 ppm. The quality of the fitting process was represented by the Cramer-Rao lower bounds (CRLBs) for each metabolite from the basis sets. Results from the LCModel fit were used to create metabolite maps and maps of spectral quality parameters such as SNR, FWHM, and CRLBs of the metabolites.

2.5.3 Statistical analysis

After data processing, the maps of quality parameters were loaded into Matlab, where statistical analysis was performed to prove that the odMRSI improves spectral properties and the quality of LCModel fit, represented by CRLBs. The statistical analysis was performed on five metabolites: inositol, glutamate, creatine, choline, N-acetyl aspartic acid. Because the odMRSI is a voxelwise method, paired tests can prove if the difference between the cases

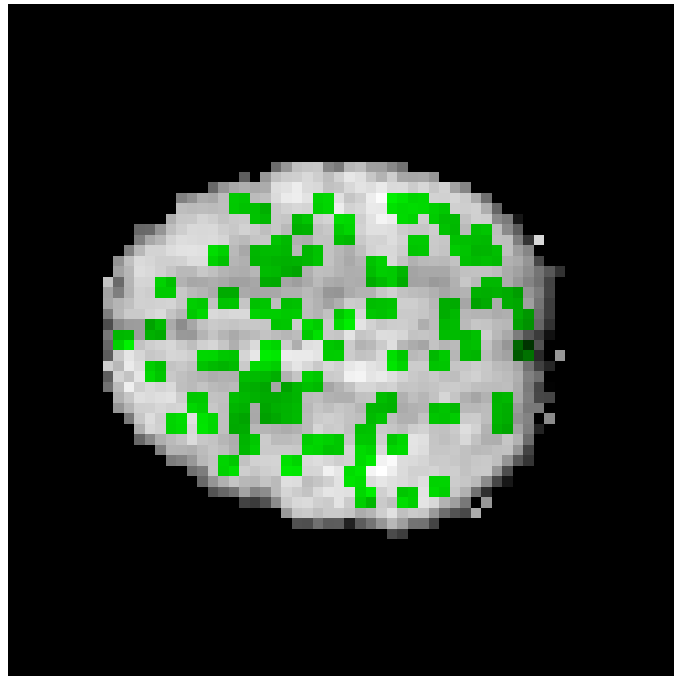


FIGURE 2.7: Metabolic map of total creatine with randomly sampled mask for statistical analysis.

before and after odMRSI is equal to zero or not. Paired t-tests or Wilcoxon sign rank tests were used for this purpose. Paired t-test requires normally distributed differences between the pairs, which was tested by the Anderson-Darling test. If this was not the case, the Wilcoxon sign test was performed.

To prove that the odMRSI improves the spectral parameters and CRLBs, the statistical analysis was performed on the data of five volunteers. Approximately 100 voxels were randomly chosen from each volunteer. The voxels were chosen only from the regions where CRLBs of metabolites were under 20%. For the comparison of the odMRSI with the Signal averaging approach, the data of volunteer number six were used. The statistical analysis was performed only on randomly sampled voxels, which were chosen in the same way as in the previous case.

The data were presented via boxplots. For SNR and FWHM, the data were depicted in the absolute numbers and also in ratios of improvement when comparing with a single measurement without odMRSI reconstruction or the Signal averaging.

Chapter 3

Results

3.1 Results of Simulations

3.1.1 Simulation results for odMRSI

The result of the simulation of the odMRSI reconstruction are presented in the table 3.1, in form of a mean and standard deviation. The first part of table 3.2 contains the result of the statistical comparison of the dataset from the simulation of odMRSI reconstruction. Figure 3.1 depicts the boxplots of the SNR increase after applying the odMRSI or the Signal averaging in percentage. In the same way, the boxplots of the FWHM are depicted in figure 3.3. Maps of the SNR increase and the FWHM change are shown in figure 3.2 and 3.4.

The SNR increased after the odMRSI and also after the Signal averaging. However the increase of the SNR is higher for the Signal averaging comparing with odMRSI with the measured B0 map (p-value < 0.001). In terms of the SNR, there is no difference between the odMRSI with the measured B0 map versus the odMRSI with the modified B0 map (p-value 0.82). The odMRSI with random B0 map brought the higher SNR as the odMRSI with the measured B0 map (p-value < 0.001). In figure 3.2 the spatial dependency in cases of odMRSI with the measured and modified B0 map can be seen. Also in these two cases, the strong correlation of the increase of the SNR and standard deviation between the subvoxels of the B0 map was found, which is depicted in figure 3.5.

Comparing the odMRSI with the Signal averaging, the FWHM increased more in cases of odMRSI with the modified and random B0 map (p-values 0.0175 and < 0.001). There was no change in case of the measured B0 map (p-value 0.2020). Also, there were no change in the FWHM comparing the odMRSI with measured B0 map against the odMRSI with the modified and random B0 map (p-values 0.0316 and < 0.001).

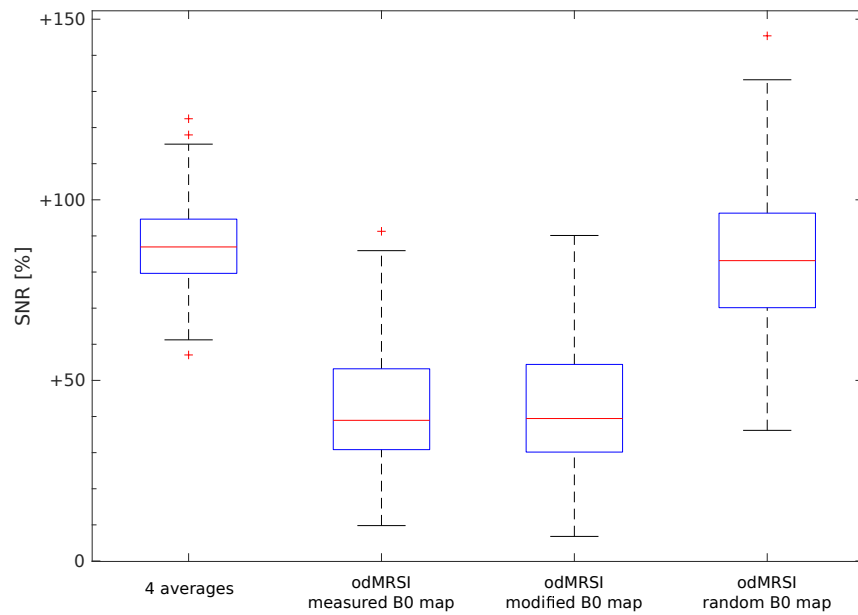


FIGURE 3.1: Boxplots of the SNR increase in percentage for the odMRSI simulation against the reference case (no averaging, no odMRSI reconstruction).

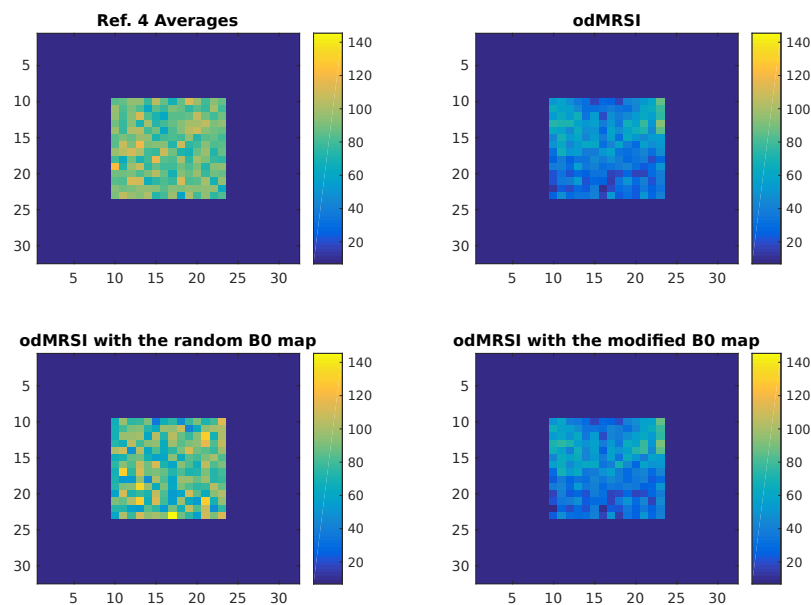


FIGURE 3.2: Maps of the SNR increase in percentage for the odMRSI simulation against the reference case (no averaging, no odMRSI reconstruction).

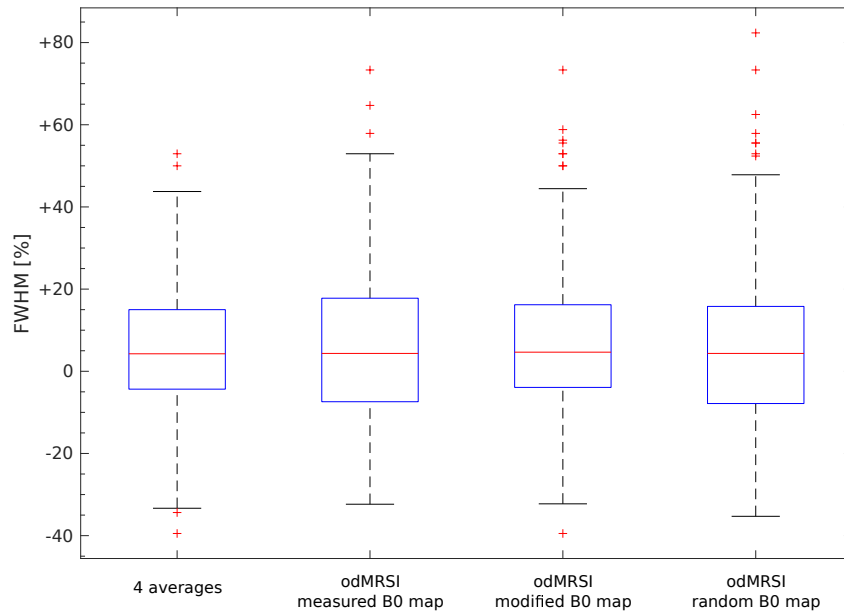


FIGURE 3.3: Boxplots of the FWHM increase in percentage for the odMRSI simulation against the reference case.

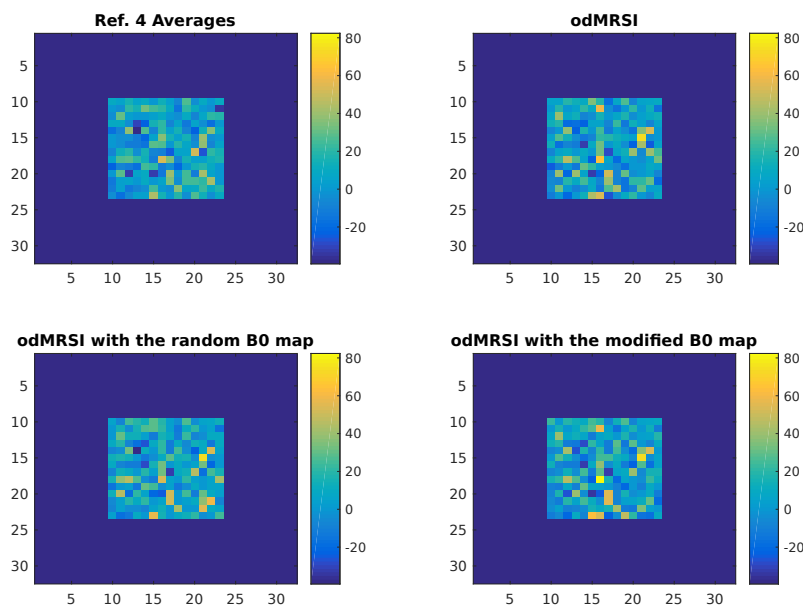


FIGURE 3.4: Maps of the FWHM increase in percentage for the odMRSI simulation against the reference case.

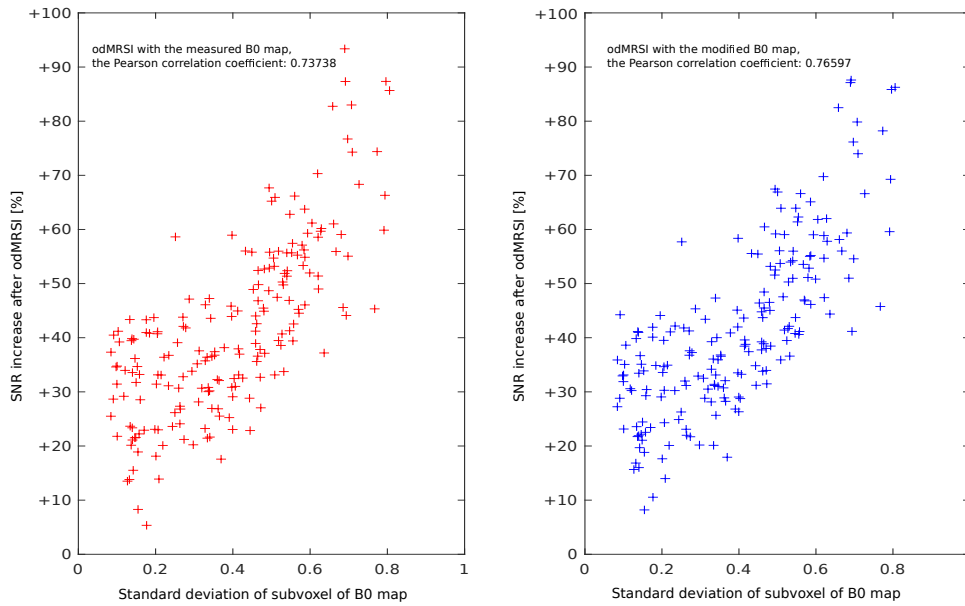


FIGURE 3.5: Plot of the standard deviation of subvoxel against the increase of the SNR after odMRSI. Left: The odMRSI with measured B0 map. Right: The odMRSI with modified B0 map.

3.1.2 Simulation results for SPREAD

The results of the simulation of the SPREAD method are presented in the last part of table 3.1, in form of a mean and standard deviation. The second part of table 3.2 contains the result of the statistical comparison of the dataset from the simulation of the SPREAD method. Figure 3.6 depicts the boxplots of the increase of the SNR in percentage after applying the SPREAD method, the Signal averaging and the Wiener-Gaussian filter. In the same way, the boxplots of the FWHM are depicted in figure 3.8. Maps of the increase of the SNR and the FWHM are in figure 3.7 and 3.9.

The SNR increased in both cases, after applying the SPREAD method and after applying the Wiener-Gaussian filter. Comparing the 4 averages with these two methods, the 4 averages yielded higher SNR values (p-value < 0.001), but there was no difference between the 4 averages and the Wiener-Gaussian filter (p-value 0.5697). The SNR after the Wiener-Gaussian filter was higher than in case of SPREAD method (p-value < 0.001). The SPREAD method increased the FWHM more than the 4 averages (p-value < 0.001) but after the Wiener-Gaussian filter the FWHM was even higher (p-value < 0.001). The spatial dependency can be seen only in case of the SNR in figure 3.7 for the SPREAD method and also for the Wiener-Gaussian filter.

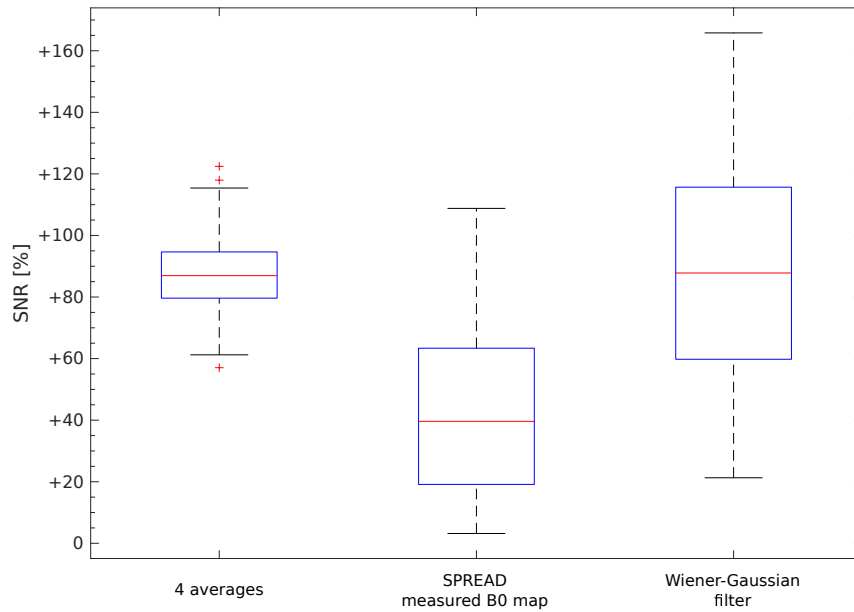


FIGURE 3.6: Boxplots of the SNR increase in percentage for the SPREAD simulation against the reference case.

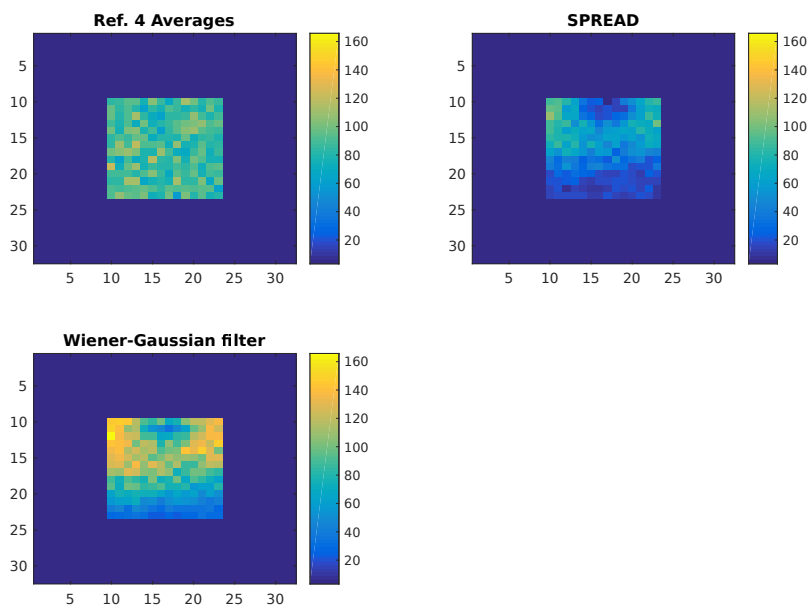


FIGURE 3.7: Maps of the SNR increase in percentage for the SPREAD simulation against the reference case.

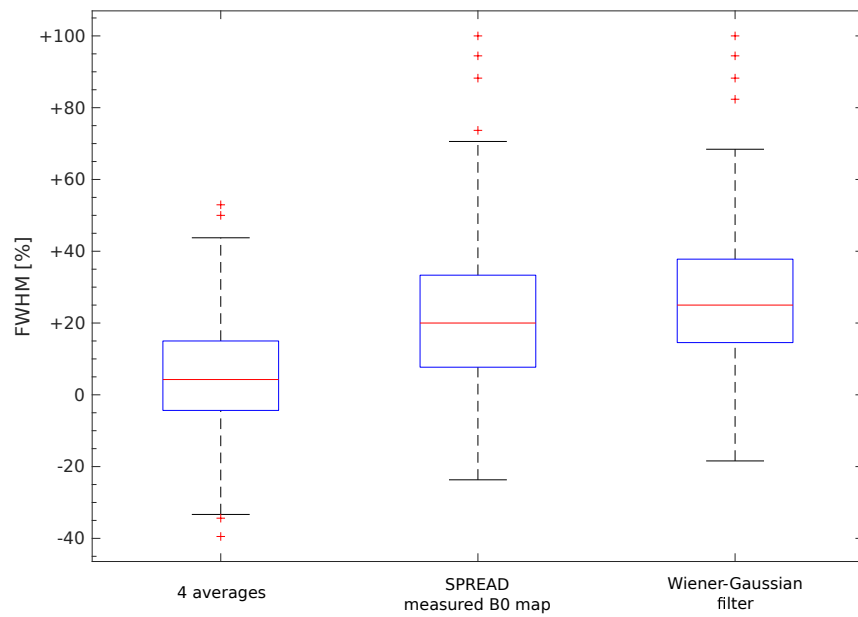


FIGURE 3.8: Boxplots of the FWHM increase in percentage for the SPREAD simulation against the reference case.

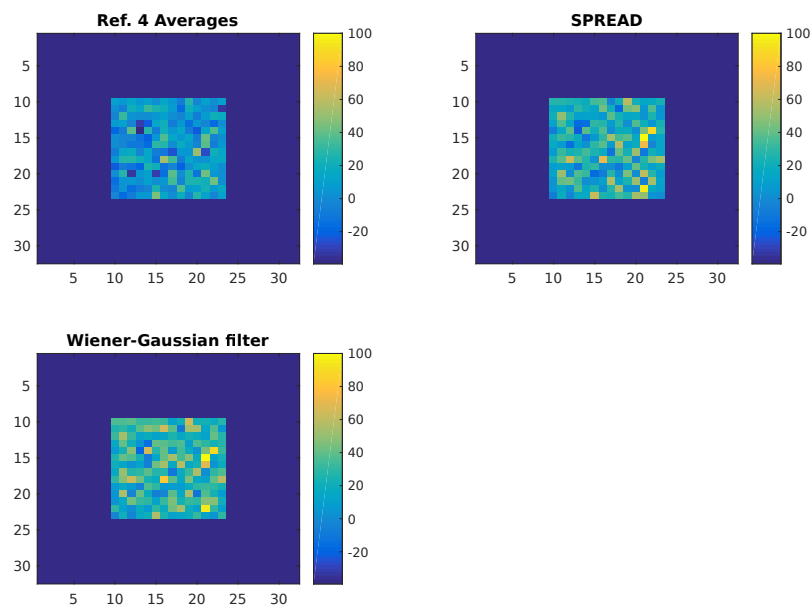


FIGURE 3.9: Maps of the FWHM increase in percentage for the SPREAD simulation against the reference case.

TABLE 3.1: The data for the statistical analysis of the simulations. The table contains the mean and the standard deviation of the SNR and the FWHM.

Spectral properties	no odMRSI	4 averages	odMRSI			SPREAD	Wiener-Gaussian filter
			measured B0 map	modified B0 map	random B0 map		
SNR	12.28 (± 0.94)	23.32 (± 1.44)	17.40 (± 1.88)	17.39 (± 1.86)	22.97 (± 1.92)	17.06 (± 3.27)	23.10 (± 4.60)
FWHM	15.19 (± 2.48)	15.52 (± 1.11)	15.71 (± 1.46)	15.84 (± 1.63)	16.05 (± 1.08)	18.19 (± 1.83)	18.92 (± 1.41)

TABLE 3.2: The result of the statistical analysis of the data from the simulations. The table contains the p-values of the Wilcoxon sign-rank.

Spectral properties	Wilcoxon sign-rank test							
	4 averages vs odMRSI with			measured vs modified B0 map	measured vs random B0 map	4 averages vs		SPREAD vs. Wiener-Gaussian filter
	measured B0 map	modified B0 map	random B0 map			SPREAD	Wiener-Gaussian filter	
SNR	< 0.001	< 0.001	0.0287	0.8229	< 0.001	< 0.001	0.5697	< 0.001
FWHM	0.2020	0.0175	< 0.001	0.0316	< 0.001	< 0.001	< 0.001	< 0.001

3.2 The results of Phantom Validation of odMRSI

The results of the phantom validation of the odMRSI as mean and standard deviation of the data before and after applying the odMRSI together with the results of the statistical comparison are presented in table 3.3. The Wilcoxon sign rank test was used for comparison, because of non-normality of the difference between the parameters before and after applying the odMRSI. Figure 3.10 depicts boxplots of the SNR and figure 3.11 depicts boxplots of the FWHM for the phantom validation. Figure 3.12 and figure 3.13 depict boxplots of the CRLBs of four fitted metabolites for the 16×16 and the 32×32 MRSI resolution, before and after applying the odMRSI.

The CRLBs of all fitted metabolites decreased after applying the odMRSI for both MRSI datasets (p-values < 0.001). However for the 16×16 MRSI dataset, there were no difference between the odMRSI with 64×64 B0 map and 128×128 B0 map. For the 32×32 MRSI dataset, the odMRSI with the 128×128 B0 map yielded lower CRLBs of Cr and GPC+PCh (p-values < 0.001). In the same case, CRLBs of Gln and NAA+NAAG were the same for both odMRSI cases (p-values 0.19 and 0.22).

For 16×16 MRSI datasets the SNR increased after applying the odMRSI with both 64×64 and 128×128 resolution B0 maps, from 70.09 (± 34.8) to 157.51 (± 44.32) and 175.60 (± 55.40) (p-values < 0.001). For the 32×32 MRSI dataset the SNR after applying the odMRSI with the same B0 maps increased from 58.08 (± 21.91) to 91.67 (± 23.57) and 115.04 (± 31.74) (p-values < 0.001). The increase after the odMRSI with 128×128 was higher (p-value < 0.001).

The FWHM increased after applying the odMRSI in all cases. For the 16×16 MRSI dataset the FWHM increased after applying the odMRSI with the 64×64 B0 map from 0.061 (± 0.0029) to 0.062 (± 0.027) (p-value 0.019) and after applying the odMRSI with the 32×32 B0 map to 0.063 (0.026) (p-value < 0.001). For the 32×32 MRSI dataset the FWHM increased after applying the odMRSI with the 64×64 B0 map from 0.036 (± 0.019) to (0.037 \pm 0.020) (p-value 0.003) and after applying the odMRSI with the 32×32 B0 map to 0.037 (± 0.020) (p-value < 0.001). There was no difference in the FWHM between odMRSI with 64×64 and 128×128 B0 map (p-value 0.33).

TABLE 3.3: The results of the statistical analysis for phantom validation. The left part of the table contains the mean and the standard deviation of the CRLBs of fitted metabolites, the SNR and the FWHM. The right part contains the p-values of the Wilcoxon sign-rank.

		odMRSI		Wilcoxon sign-rank test		
		B0 map 64res.	B0 map 128res.	noOD vs OD64	noOD vs OD128	OD64 vs OD128
MRSI 16x16 resolution						
metabolite	mean \pm SD					
CLRB Cr [%]	3.39 \pm 0.83	2.72 \pm 0.74	2.66 \pm 0.87	< 0.001	< 0.001	0.1349
CLRB Gln [%]	11.53 \pm 3.50	8.93 \pm 4.71	8.83 \pm 4.85	< 0.001	< 0.001	0.3861
CLRB GPC+PCh [%]	3.41 \pm 0.70	2.90 \pm 0.86	2.87 \pm 0.97	< 0.001	< 0.001	0.3742
CLRB NAA+NAAG [%]	2.47 \pm 0.56	2.17 \pm 0.59	2.15 \pm 0.72	< 0.001	< 0.001	0.6367
spectral properties						
SNR	70.09 \pm 34.38	157.51 \pm 44.32	175.60 \pm 55.40	< 0.001	< 0.001	< 0.001
FWHM [ppm]	0.061 \pm 0.029	0.062 \pm 0.027	0.063 \pm 0.026	0.019	< 0.001	0.0324
MRSI 32x32 resolution						
metabolite						
CLRB Cr [%]	3.28 \pm 0.45	2.95 \pm 0.28	2.73 \pm 0.48	< 0.001	< 0.001	< 0.001
CLRB Gln [%]	17.09 \pm 1.38	12.55 \pm 2.46	12.27 \pm 2.76	< 0.001	< 0.001	0.1902
CLRB GPC+PCh [%]	3.50 \pm 0.56	2.88 \pm 0.47	2.66 \pm 0.56	< 0.001	< 0.001	< 0.001
CLRB NAA+NAAG [%]	2.53 \pm 0.50	2.08 \pm 0.28	2.05 \pm 0.23	< 0.001	< 0.001	0.2188
spectral properties						
SNR	58.08 \pm 21.91	91.67 \pm 23.57	115.04 \pm 31.74	< 0.001	< 0.001	< 0.001
FWHM [ppm]	0.036 \pm 0.019	0.037 \pm 0.020	0.037 \pm 0.020	0.003	< 0.001	0.3311

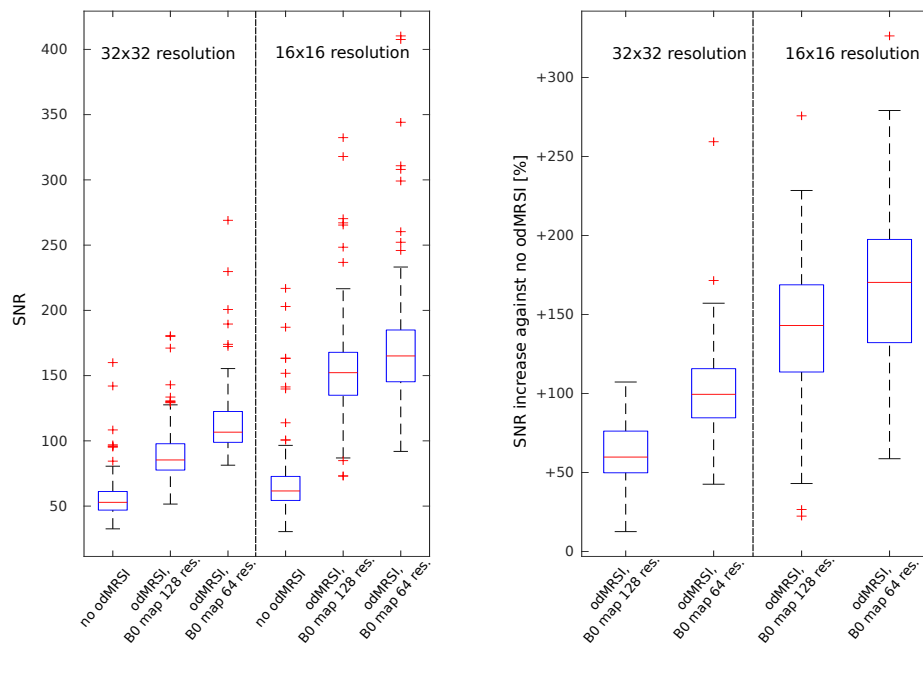


FIGURE 3.10: Boxplots of the SNR for the phantom validation of the odMRSI. Left: Boxplots of the absolute values of the SNR. Right: Boxplots of the SNR increase in percentage after applying the odMRSI reconstruction.

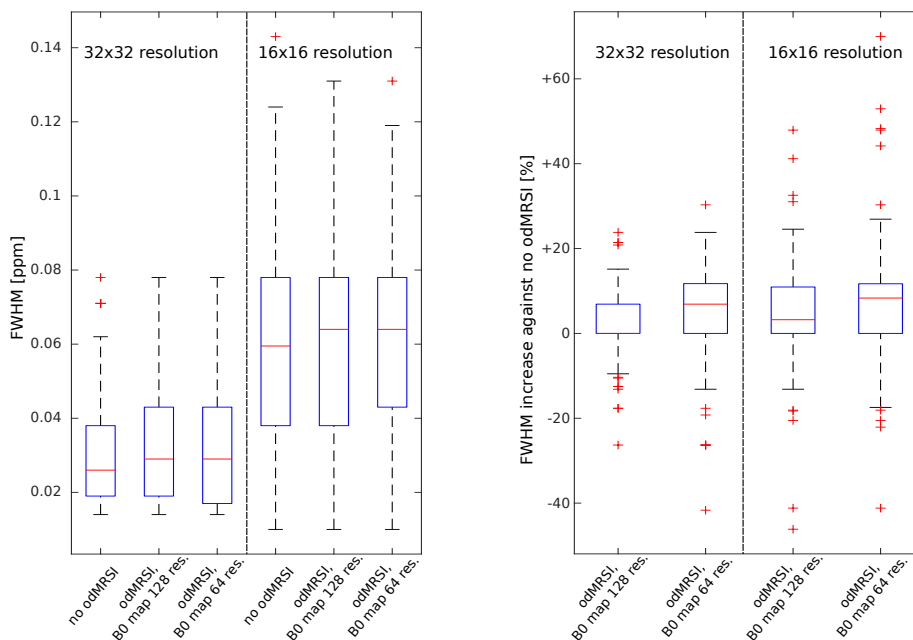


FIGURE 3.11: Boxplots of the FWHM for the phantom validation of the odMRSI. Left: Boxplots of the absolute values of the FWHM. Right: Boxplots of the FWHM increase in percentage after applying the odMRSI reconstruction.

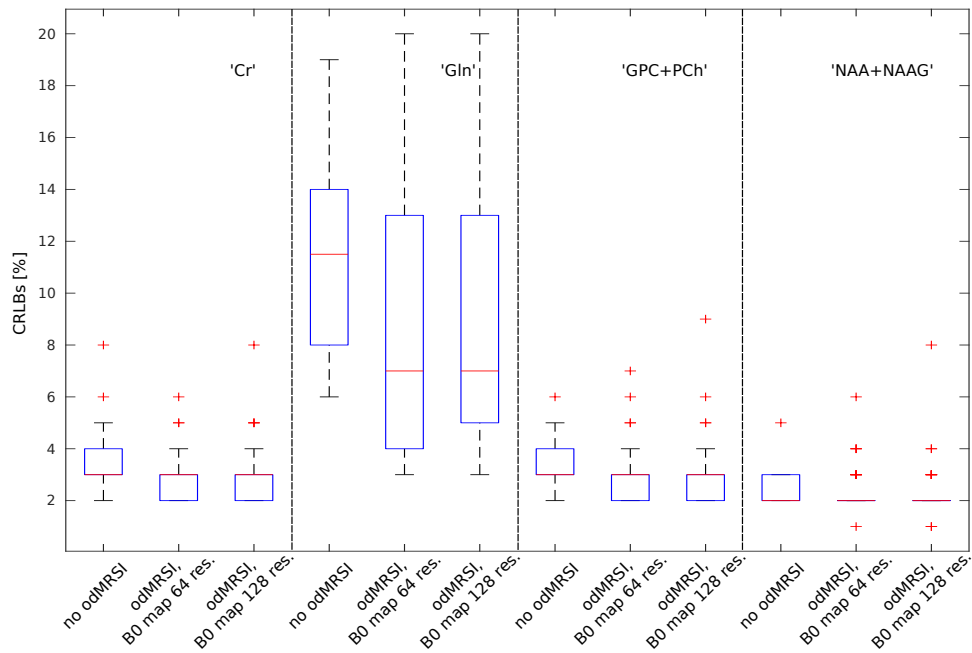


FIGURE 3.12: Boxplots of the CRLBs of the fitted metabolites for phantom validation of odMRSI, performed on the 16×16 resolution MRSI data.

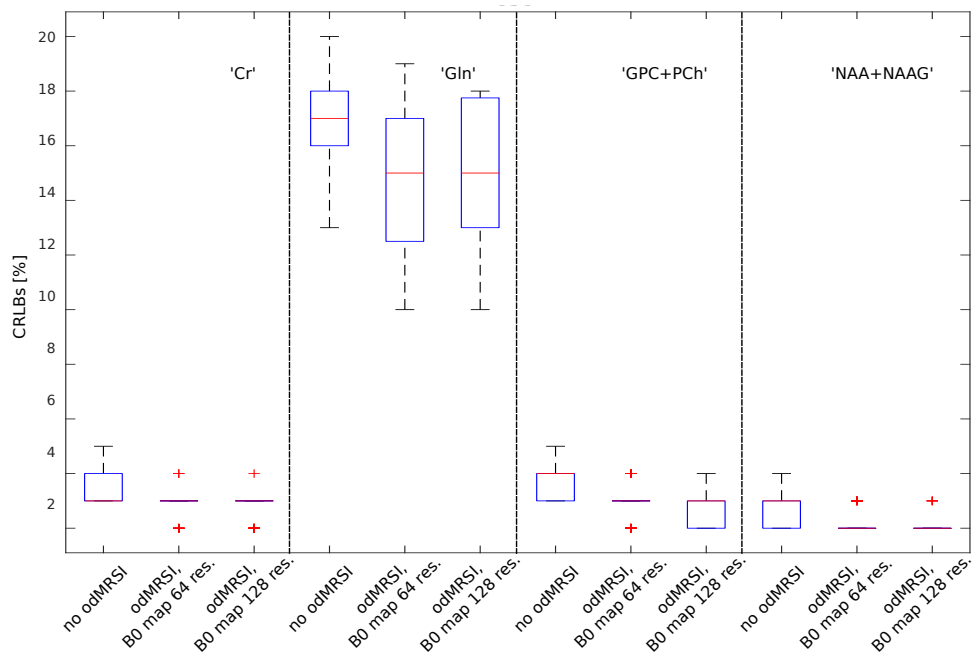


FIGURE 3.13: Boxplots of the CRLBs of the fitted metabolites for phantom validation of odMRSI, performed on the 32×32 resolution MRSI data.

3.3 The results of inVivo validation

Table 3.4 contains data for inVivo validation of odMRSI. In the first part of the table are means and standard deviations of CRLBs of the fitted metabolites, the SNR and the FWHM for the cases before and after applying the odMRSI. The second part of the table contains the results of the statistical comparison of the parameters before and after applying the odMRSI reconstruction. The right part of the table 3.7 contains the results from comparing the odMRSI with different resolution of B0 map. The Wilcoxon sign rank test was used because of non-normality of differences between tested data. Figure 3.14 depicts the boxplots of the absolute values of the SNR before and after the odMRSI and of the SNR increase after applying the odMRSI. In the same manner, figure 3.15 depicts the results for the FWHM. Figure 3.16 and figure 3.17 depict the boxplots of the CRLBs of the fitted metabolites for the MRSI resolution of 64×64 and 100×100 .

The CRLBs of all fitted metabolites decreased after applying the odMRSI with three different resolution of B0 map for the 64×64 resolution of MRSI dataset and also for the 100×100 resolution of MRSI dataset (p-values < 0.001). The lowest CRLBs values were achieved with the odMRSI with 400×400 B0 map for both MRSI datasets (p-values < 0.001).

For 64×64 MRSI dataset, the SNR 7.78 ± 2.86 increased after applying the odMRSI with 200×200 B0 map to 11.68 ± 3.81 (p-value < 0.001), after applying the odMRSI with 300×300 B0 map to 13.10 ± 4.00 (p-value < 0.001) and after applying the odMRSI with 400×400 B0 map to 14.15 ± 4.07 (p-value < 0.001). For 100×100 MRSI dataset, the SNR 5.17 ± 2.57 increased after applying the odMRSI with 200×200 B0 map to 7.50 ± 3.48 (p-value < 0.001) and after applying the odMRSI with 300×300 B0 map to 8.75 ± 4.03 (p-value < 0.001). The odMRSI with 400×400 B0 map increased the SNR to 10.03 ± 4.36 (p-value < 0.001), which was the highest SNR value (p-values < 0.001).

For 64×64 MRSI dataset, the FWHM 0.05 ± 0.02 increased after applying the odMRSI in all three cases with different resolution of B0 map to 0.05 ± 0.03 (p-values < 0.001). For 100×100 MRSI dataset, the FWHM 0.06 ± 0.04 increased after applying the odMRSI with 200×200 and 300×300 resolution of B0 map to 0.07 ± 0.04 (p-values < 0.001). However, after applying the odMRSI with 200×200 B0 map the FWHM was not changed (p-value 0.44).

TABLE 3.4: The results of the statistical analysis for in vivo validation of odMRSI reconstruction. The left part of the table contains the mean and the standard deviation of the CRLBs of fitted metabolites, the SNR and the FWHM. The right part contains the p-values of the Wilcoxon sign-rank from the comparing the data before and after odMRSI reconstruction.

	no odMRSI	odMRSI			Wilcoxon sign-rank test		
		B0 200res.	map 300res.	map 400res.	no odMRSI vs odMRSI200	no odMRSI vs odMRSI300	no odMRSI vs odMRSI400
MRSI 64x64 res.	mean \pm SD						
CRBL Ins [%]	12.21 \pm 3.69	7.83 \pm 2.44	6.99 \pm 2.02	6.41 \pm 1.70	< 0.001	< 0.001	< 0.001
CRBL Glu [%]	7.07 \pm 2.74	5.11 \pm 2.07	4.63 \pm 1.86	4.30 \pm 1.61	< 0.001	< 0.001	< 0.001
CRBL GPC+PCh [%]	5.86 \pm 1.95	4.49 \pm 1.47	4.18 \pm 1.48	3.98 \pm 1.40	< 0.001	< 0.001	< 0.001
CRBL NAA+NAAG [%]	4.16 \pm 1.59	3.07 \pm 1.39	2.82 \pm 1.31	2.69 \pm 1.06	< 0.001	< 0.001	< 0.001
CRBL Cr+PCr [%]	5.63 \pm 1.71	4.25 \pm 1.33	3.89 \pm 1.14	3.71 \pm 1.29	< 0.001	< 0.001	< 0.001
SNR	7.78 \pm 2.86	11.68 \pm 3.81	13.10 \pm 4.00	14.15 \pm 4.07	< 0.001	< 0.001	< 0.001
FWHM [ppm]	0.05 \pm 0.02	0.05 \pm 0.03	0.05 \pm 0.03	0.05 \pm 0.03	< 0.001	< 0.001	< 0.001
MRSI 100x100 res.							
CRBL Ins [%]	14.65 \pm 3.71	10.39 \pm 3.10)	8.79 \pm 2.56	7.75 \pm 2.24	< 0.001	< 0.001	< 0.001
CRBL Glu [%]	9.57 \pm 3.75	7.21 \pm 3.07	6.40 \pm 2.64	5.83 \pm 2.55	< 0.001	< 0.001	< 0.001
CRBL GPC+PCh [%]	8.08 \pm 2.75	6.31 \pm 2.17	5.69 \pm 2.06	5.22 \pm 1.98	< 0.001	< 0.001	< 0.001
CRBL NAA+NAAG [%]	6.30 \pm 2.56	4.78 \pm 2.02	4.22 \pm 1.73	3.82 \pm 1.70	< 0.001	< 0.001	< 0.001
CRBL Cr+PCr [%]	7.68 \pm 2.45	6.10 \pm 2.09	5.47 \pm 1.87	5.07 \pm 2.06	< 0.001	< 0.001	< 0.001
SNR	5.17 \pm 2.57	7.50 \pm 3.48	8.75 \pm 4.03	10.03 \pm 4.36	< 0.001	< 0.001	< 0.001
FWHM [ppm]	0.06 \pm 0.04	0.06 \pm 0.04	0.07 \pm 0.04	0.07 \pm 0.04	0.4386	< 0.001	< 0.001

TABLE 3.5: The results of the statistical analysis for in vivo validation of odMRSI reconstruction. The left part of the table contains the mean and the standard deviation of the CRLBs of fitted metabolites, the SNR and the FWHM. The right part contains the p-values of the Wilcoxon sign-rank from the comparing the odMRSI with different resolution of B0 map .

	no odMRSI	odMRSI			Wilcoxon sign-rank test		
		B0 map 200res.	B0 map 300res.	B0 map 400res.	odMRSI200 vs odMRSI300	odMRSI200 vs odMRSI400	odMRSI300 vs odMRSI400
MRSI 64x64 res.		mean \pm SD					
CRBL Ins [%]	12.21 \pm 3.69	7.83 \pm 2.44	6.99 \pm 2.02	6.41 \pm 1.70	< 0.001	< 0.001	< 0.001
CRBL Glu [%]	7.07 \pm 2.74	5.11 \pm 2.07	4.63 \pm 1.86	4.30 \pm 1.61	< 0.001	< 0.001	< 0.001
CRBL GPC+PCh [%]	5.86 \pm 1.95	4.49 \pm 1.47	4.18 \pm 1.48	3.98 \pm 1.40	< 0.001	< 0.001	< 0.001
CRBL NAA+NAAG [%]	4.16 \pm 1.59	3.07 \pm 1.39	2.82 \pm 1.31	2.69 \pm 1.06	< 0.001	< 0.001	< 0.001
CRBL Cr+PCr [%]	5.63 \pm 1.71	4.25 \pm 1.33	3.89 \pm 1.14	3.71 \pm 1.29	< 0.001	< 0.001	< 0.001
SNR	7.78 \pm 2.86	11.68 \pm 3.81	13.10 \pm 4.00	14.15 \pm 4.07	< 0.001	< 0.001	< 0.001
FWHM [ppm]	0.05 \pm 0.02	0.05 \pm 0.03	0.05 \pm 0.03	0.05 \pm 0.03	< 0.001	< 0.001	< 0.001
MRSI 100x100 res.							
CRBL Ins [%]	14.65 \pm 3.71	10.39 \pm 3.10	8.79 \pm 2.56	7.75 \pm 2.24	< 0.001	< 0.001	< 0.001
CRBL Glu [%]	9.57 \pm 3.75	7.21 \pm 3.07	6.40 \pm 2.64	5.83 \pm 2.55	< 0.001	< 0.001	< 0.001
CRBL GPC+PCh [%]	8.08 \pm 2.75	6.31 \pm 2.17	5.69 \pm 2.06	5.22 \pm 1.98	< 0.001	< 0.001	< 0.001
CRBL NAA+NAAG [%]	6.30 \pm 2.56	4.78 \pm 2.02	4.22 \pm 1.73	3.82 \pm 1.70	< 0.001	< 0.001	< 0.001
CRBL Cr+PCr [%]	7.68 \pm 2.45	6.10 \pm 2.09	5.47 \pm 1.87	5.07 \pm 2.06	< 0.001	< 0.001	< 0.001
SNR	5.17 \pm 2.57	7.50 \pm 3.48	8.75 \pm 4.03	10.03 \pm 4.36	< 0.001	< 0.001	< 0.001
FWHM [ppm]	0.06 \pm 0.04	0.06 \pm 0.04	0.07 \pm 0.04	0.07 \pm 0.04	< 0.001	< 0.001	< 0.001

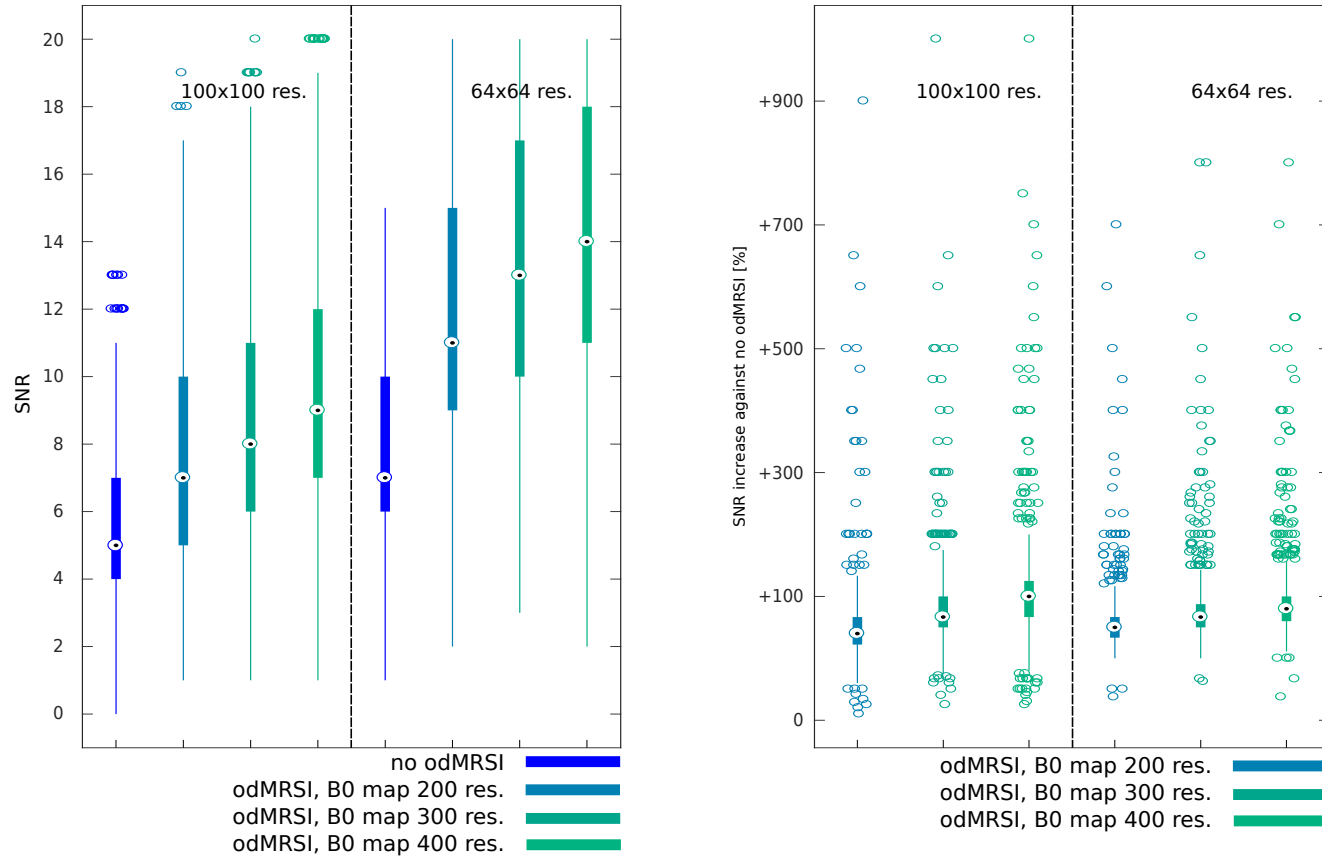


FIGURE 3.14: Boxplots of the SNR from the in vivo validation of the odMRSI. Left: Boxplots of the absolute values of the SNR. Right: Boxplots of the SNR increase after applying the odMRSI reconstruction.

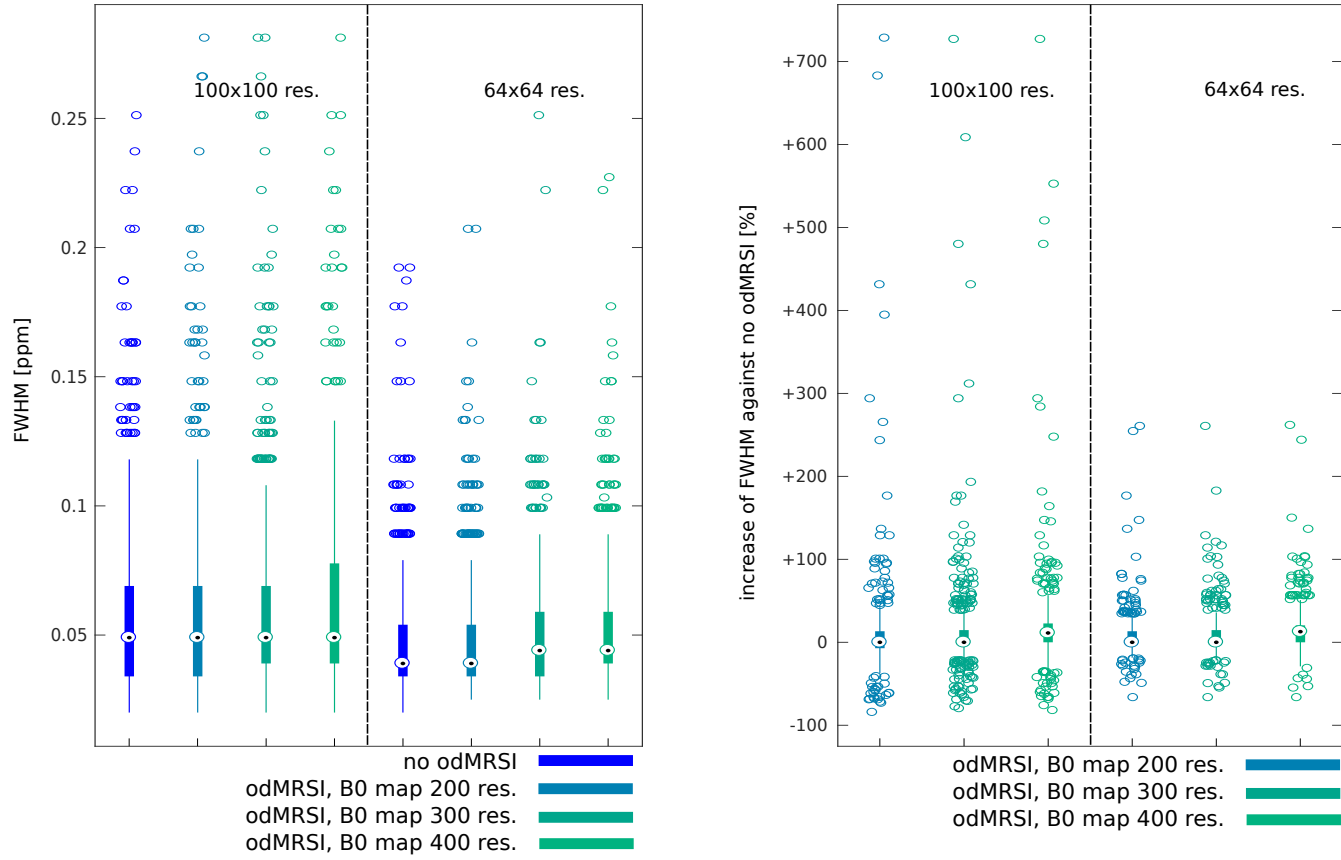


FIGURE 3.15: Boxplots of the FWHM from the in vivo validation of the odMRSI. Left: Boxplots of the absolute values of the FWHM. Right: Boxplots of the FWHM increase after applying the odMRSI reconstruction.

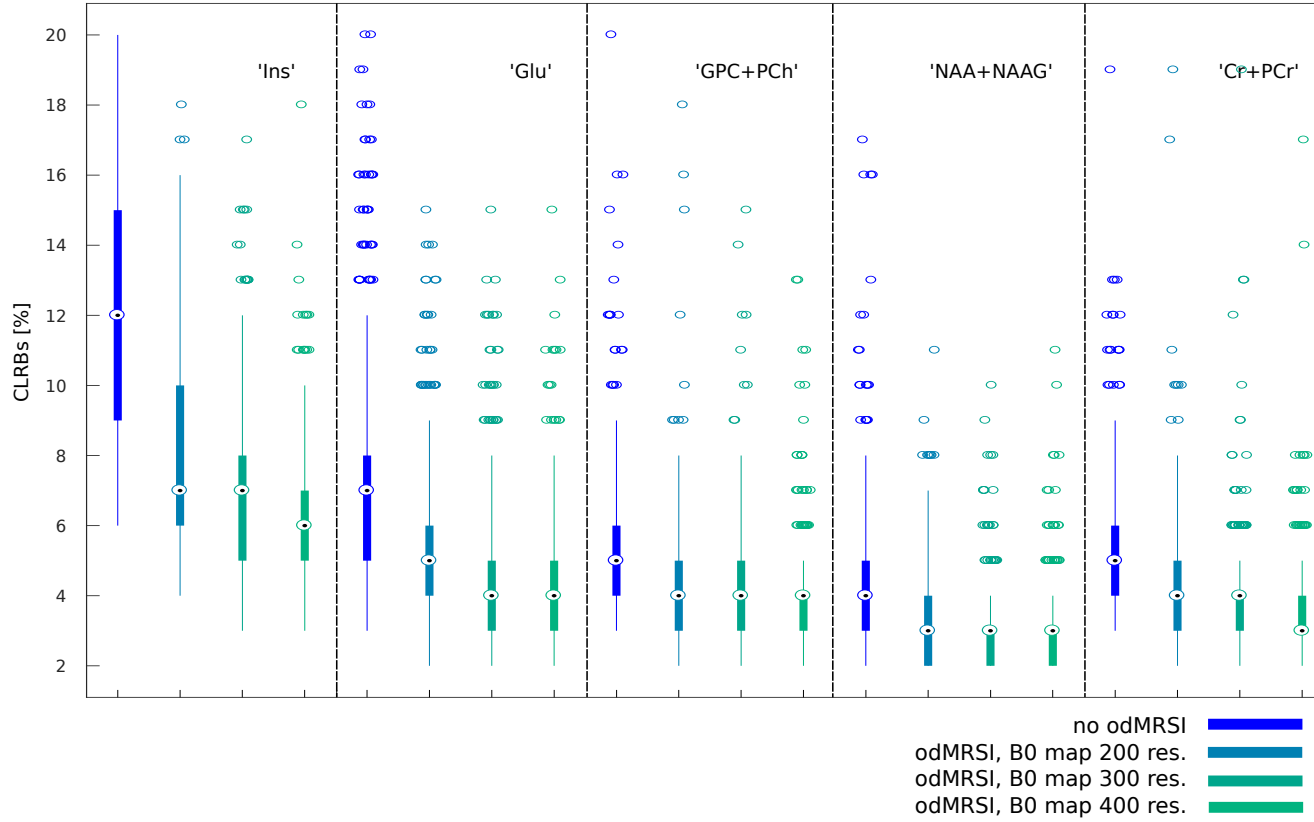


FIGURE 3.16: Boxplots of the CRLBs of the fitted metabolites for in vivo validation of odMRSI, performed on the 64×64 resolution MRSI data.

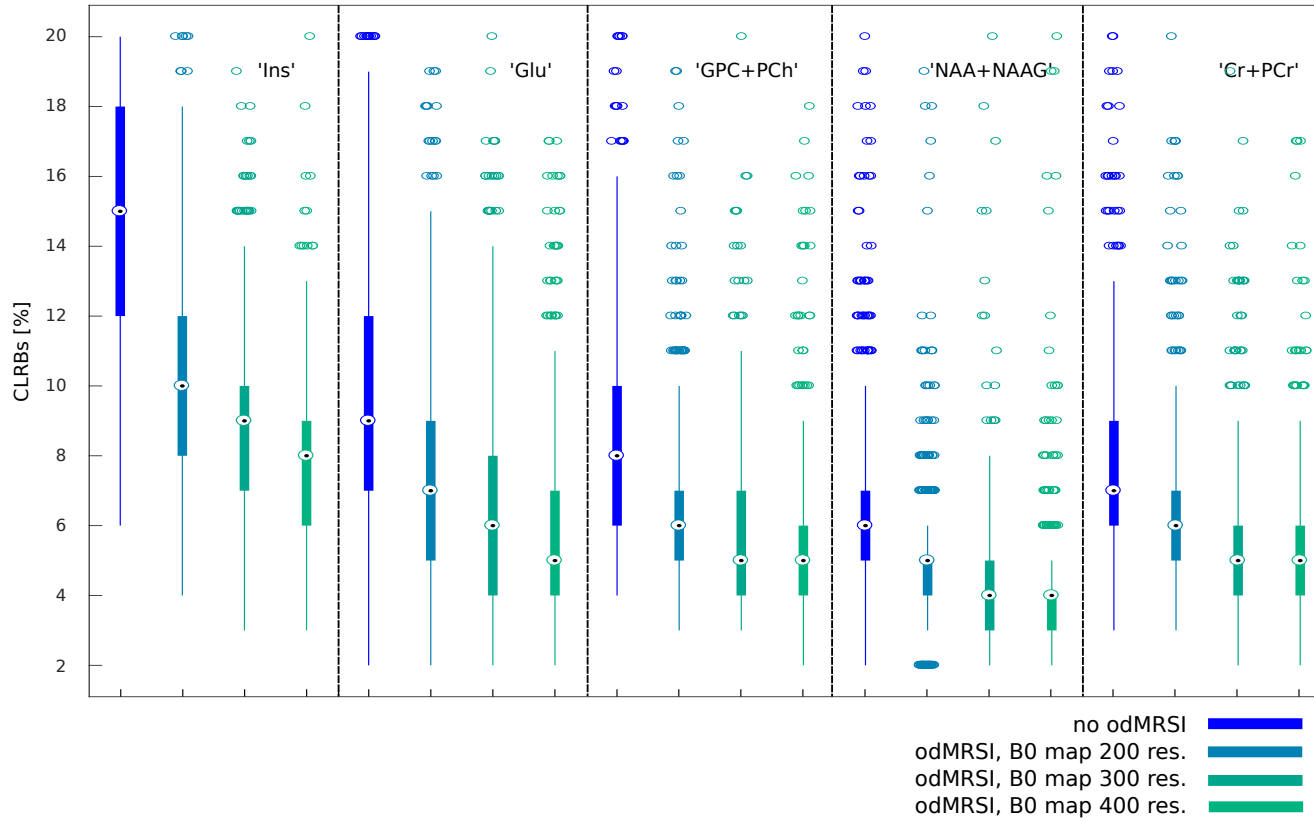


FIGURE 3.17: Boxplots of the CRLBs of the fitted metabolites for in vivo validation of odMRSI, performed on the 100×100 resolution MRSI data.

3.4 The result of validation of odMRSI against signal averaging

The result of comparison between the odMRSI and the Signal averaging in the in vivo data are presented in table 3.6 for 4 averages and 5 averages and in table 3.7 for 6 averages Figure 3.18 depicts the boxplots of the SNR for the visual comparison of the odMRSI and the Signal averaging in absolute values and as the increase of the SNR after applying the odMRSI or the Signal averaging. The results of the FWHM are presented in the same way in figure 3.19. Figure 3.20 depicts the boxplots of the CRLBs of the fitted metabolites before applying the odMRSI or the Signal averaging and after applying these two methods.

Comparing the results after the Signal averaging with the results after the odMRSI, the odMRSI with 400×400 B0 map yielded lower CRLBs of the fitted metabolites than 4 averages and 5 averages (p-values < 0.001). Also, the SNR after the 4 averages was lower than after the odMRSI with 300×300 B0 map (p-value < 0.001). The SNR after the 5 averages was overcome with the odMRSI with 400×400 B0 map (p-value < 0.001). However, the CRLBs of the fitted metabolites after the odMRSI with 400×400 B0 map was lower than after the 6 averages only for Ins, GPC+PCh and NAA+NAAG (p-value < 0.001) and for Glu and Cr+PCr there was no difference (p-values 0.84 and 0.05). Additionally, the SNR after the odMRSI with 400×400 B0 map and the 6 averages was the same (p-value 0.07). The Signal averaging yielded consistently to the lower FWHM (p-values < 0.001).

TABLE 3.6: The results of statistical analysis for comparison of the odMRSI against the Signal averaging on in vivo dataset (4 averages and 5 averages). The left part of the table contains the mean and the standard deviation of the CRLBs of fitted metabolites, the SNR and the FWHM. The right part contains the p-values of the Wilcoxon sign-rank.

		odMRSI			Wilcoxon sign-rank test		
4 averages		B0map 200res.	B0map 300res.	B0map 400res.	4aver. vs odMRSI200	4aver. vs odMRSI300	4aver. vs odMRSI400
metabolite	mean \pm SD						
CRLB Ins [%]	10.09 \pm 2.24	10.25 \pm 2.22	8.39 \pm 1.83	7.07 \pm 1.35	0.6187	< 0.001	< 0.001
CRLB Glu [%]	7.43 \pm 2.37	8.35 \pm 2.63	7.28 \pm 2.38	6.51 \pm 2.05	< 0.001	0.1801	< 0.001
CRLB GPC+PCh [%]	5.60 \pm 1.57	6.11 \pm 1.54	5.25 \pm 1.21	4.80 \pm 1.49	< 0.001	< 0.001	< 0.001
CRLB NAA+NAAG [%]	4.41 \pm 1.20	4.90 \pm 1.24	4.10 \pm 0.89	3.71 \pm 0.87	< 0.001	< 0.001	< 0.001
CRLB Cr+PCr [%]	5.55 \pm 1.43	6.26 \pm 1.86	5.48 \pm 1.59	4.94 \pm 1.36	< 0.001	0.2205	< 0.001
spectral properties							
SNR	7.29 \pm 2.30	6.29 \pm 2.05	7.54 \pm 2.36	8.70 \pm 2.88	< 0.001	< 0.001	< 0.001
FWHM [ppm]	0.04 \pm 0.02	0.05 \pm 0.03	0.05 \pm 0.03	0.05 \pm 0.03	< 0.001	< 0.001	< 0.001
5 averages		B0map 200res.	B0map 300res.	B0map 400res.	5aver. vs odMRSI200	5aver. vs odMRSI300	5aver. vs odMRSI400
metabolite							
CRLB Ins [%]	8.81 \pm 1.43	10.25 \pm 2.22	8.39 \pm 1.83	7.07 \pm 1.35	< 0.001	< 0.001	< 0.001
CRLB Glu [%]	6.86 \pm 1.79	8.35 \pm 2.63	7.28 \pm 2.38	6.51 \pm 2.05	< 0.001	< 0.001	< 0.001
CRLB GPC+PCh [%]	5.18 \pm 1.18	6.11 \pm 1.54	5.25 \pm 1.21	4.80 \pm 1.49	< 0.001	0.2829	< 0.001
CRLB NAA+NAAG [%]	4.05 \pm 0.97	4.90 \pm 1.24	4.10 \pm 0.89	3.71 \pm 0.87	< 0.001	0.4005	< 0.001
CRLB Cr+PCr [%]	5.26 \pm 1.34	6.26 \pm 1.86	5.48 \pm 1.59	4.94 \pm 1.36	< 0.001	< 0.001	< 0.001
spectral properties							
SNR	7.94 \pm 2.16	6.29 \pm 2.05	7.54 \pm 2.36	8.70 \pm 2.88	< 0.001	< 0.001	< 0.001
FWHM [ppm]	0.04 \pm 0.02	0.05 \pm 0.03	0.05 \pm 0.03	0.05 \pm 0.03	< 0.001	< 0.001	< 0.001

TABLE 3.7: The results of statistical analysis for comparison of the odMRSI against the Signal averaging on in vivo dataset (6 averages). The left part of the table contains the mean and the standard deviation of the CRLBs of fitted metabolites, the SNR and the FWHM. The right part contains the p-values of the Wilcoxon sign-rank.

		odMRSI			Wilcoxon sign-rank test		
6 averages		B0map 200res.	B0map 300res.	B0map 400res.	6aver. vs odMRSI200	6aver. vs odMRSI300	6aver. vs odMRSI400
metabolite	mean \pm SD						
CRLB Ins [%]	8.20 \pm 1.39	10.25 \pm 2.22	8.39 \pm 1.83	7.07 \pm 1.35	< 0.001	0.3972	< 0.001
CRLB Glu [%]	6.46 \pm 1.73	8.35 \pm 2.63	7.28 \pm 2.38	6.51 \pm 2.05	< 0.001	< 0.001	0.8404
CRLB GPC+PCh [%]	4.91 \pm 1.15	6.11 \pm 1.54	5.25 \pm 1.21	4.80 \pm 1.49	< 0.001	< 0.001	< 0.001
CRLB NAA+NAAG [%]	3.83 \pm 0.90	4.90 \pm 1.24	4.10 \pm 0.89	3.71 \pm 0.87	< 0.001	< 0.001	< 0.001
CRLB Cr+PCr [%]	5.00 \pm 1.14	6.26 \pm 1.86	5.48 \pm 1.59	4.94 \pm 1.36	< 0.001	< 0.001	0.0516
spectral properties							
SNR	8.53 \pm 2.40	6.29 \pm 2.05	7.54 \pm 2.36	8.70 \pm 2.88	< 0.001	< 0.001	0.0710
FWHM [ppm]	0.04 \pm 0.02	0.05 \pm 0.03	0.05 \pm 0.03	0.05 \pm 0.03	< 0.001	< 0.001	< 0.001

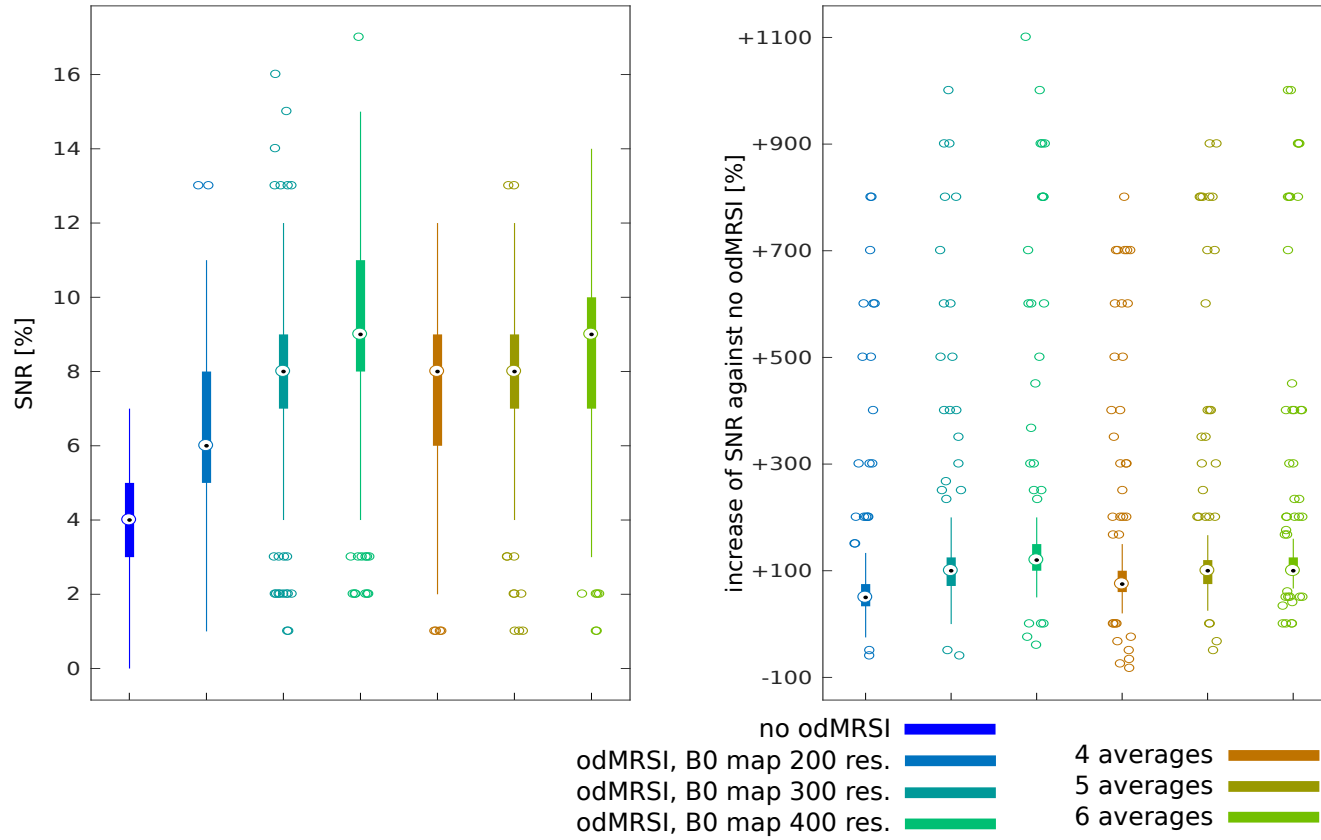


FIGURE 3.18: Boxplots of the SNR from the comparison of the odMRSI against the Signal averaging. Left: Boxplots of the absolute values of the SNR before and after applying the odMRSI and from the Signal averaging. Right: Boxplots of the SNR increase after applying the odMRSI or the Signal averaging.

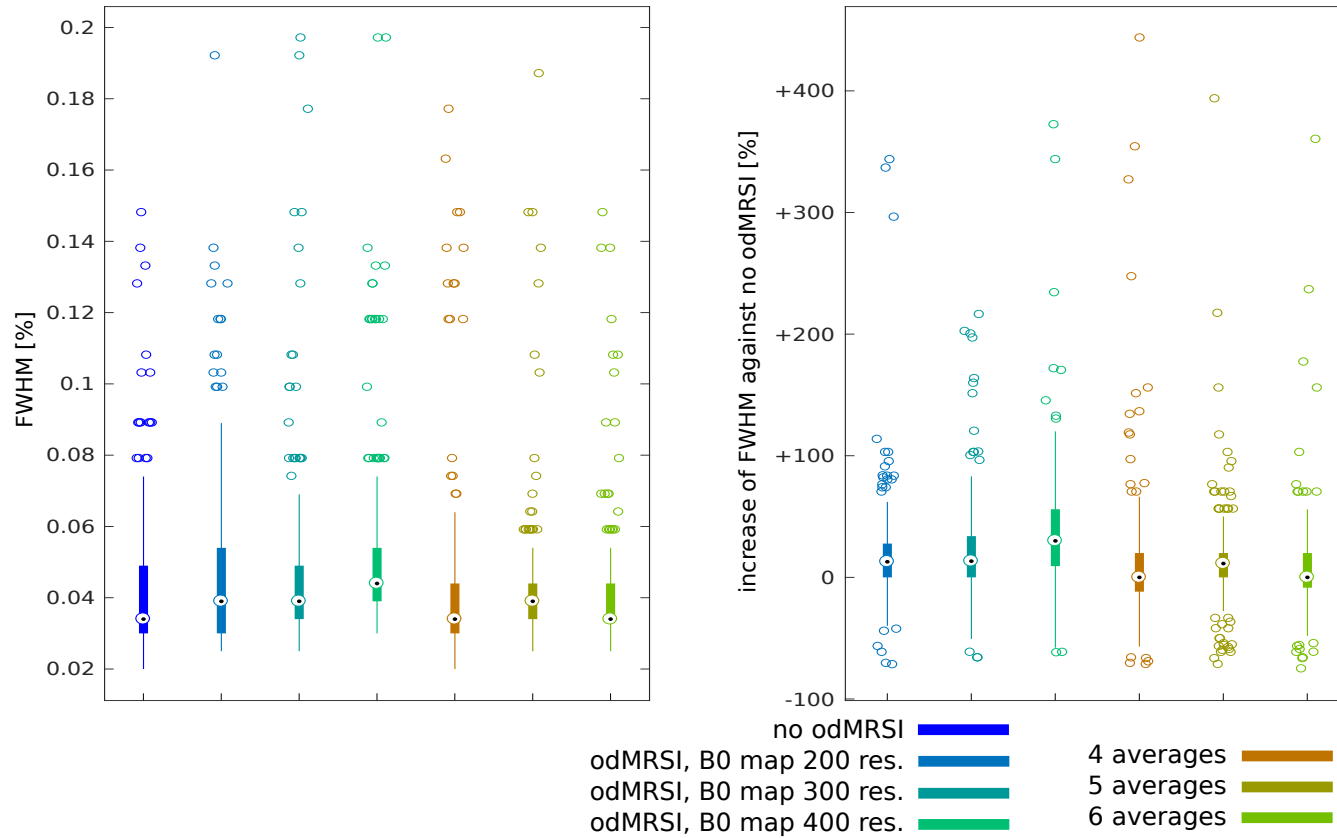


FIGURE 3.19: Boxplots of the FWHM from the comparison of the odMRSI against the Signal averaging. Left: Boxplots of the absolute values of the FWHM before and after applying the odMRSI and from the Signal averaging. Right: Boxplots of the FWHM increase after applying the odMRSI or the Signal averaging.

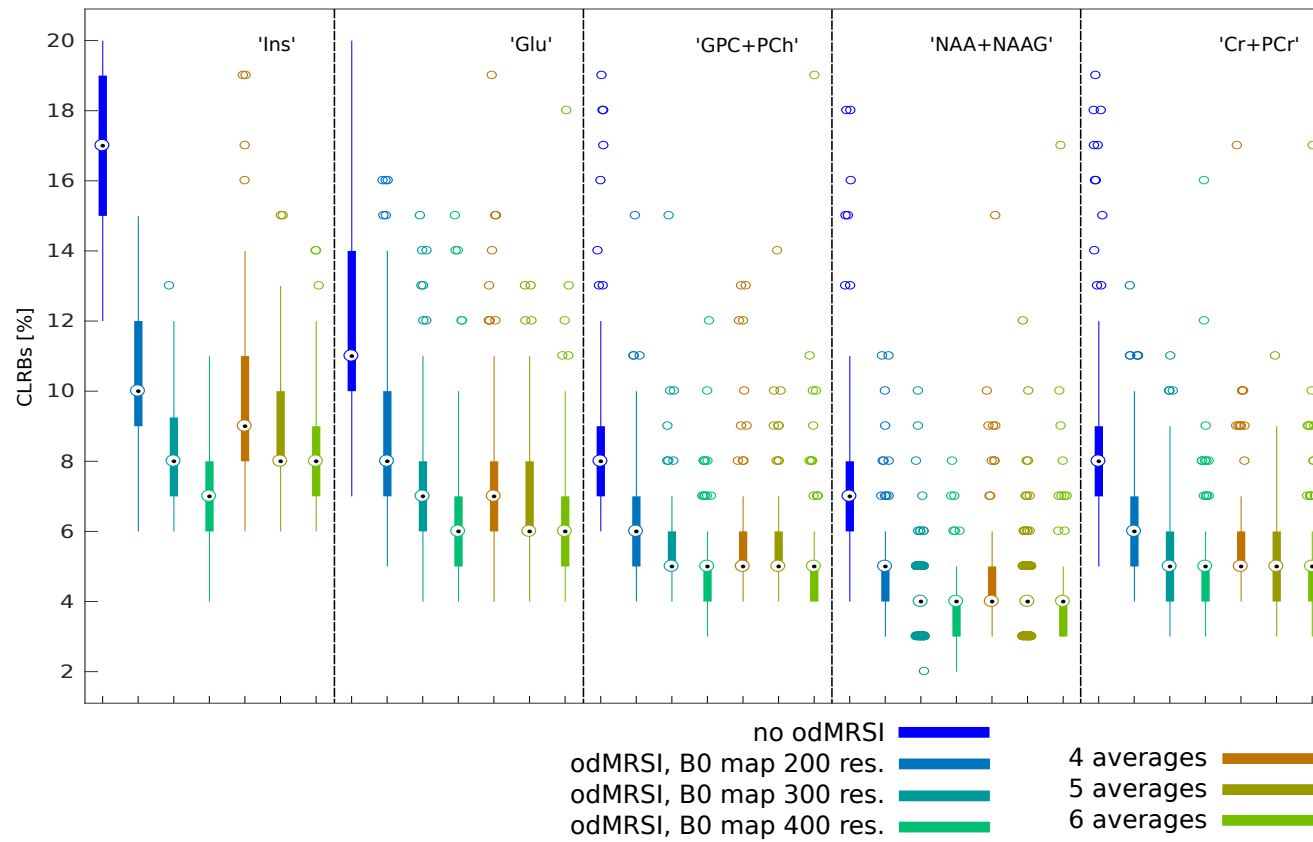


FIGURE 3.20: Boxplots of the CRLBs of the fitted metabolites for comparison of the odMRSI against the Signal averaging.

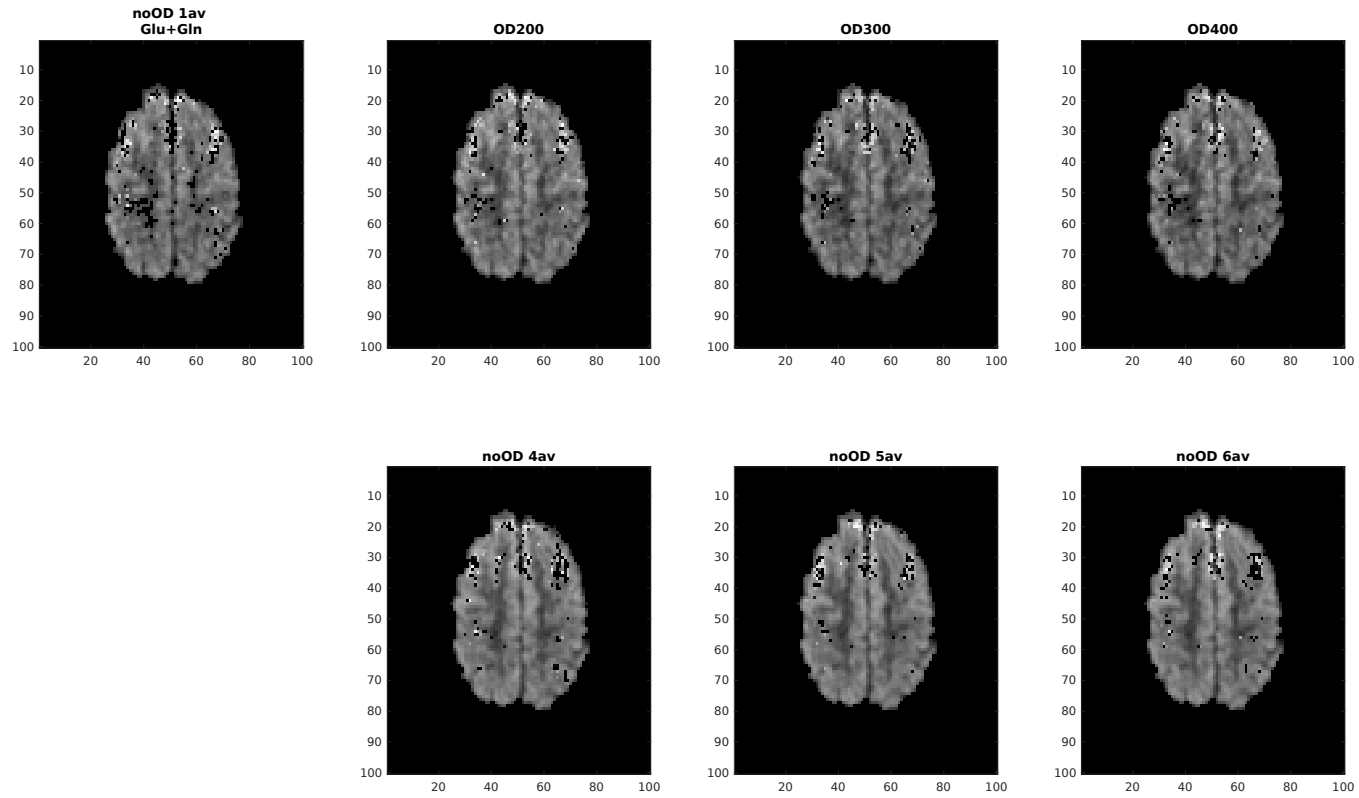


FIGURE 3.21: Comparison of metabolic maps of the Glu+Gln between the Signal averaging and the odMRSI reconstruction. Averages show visual improvement, but the odMRSI does not.

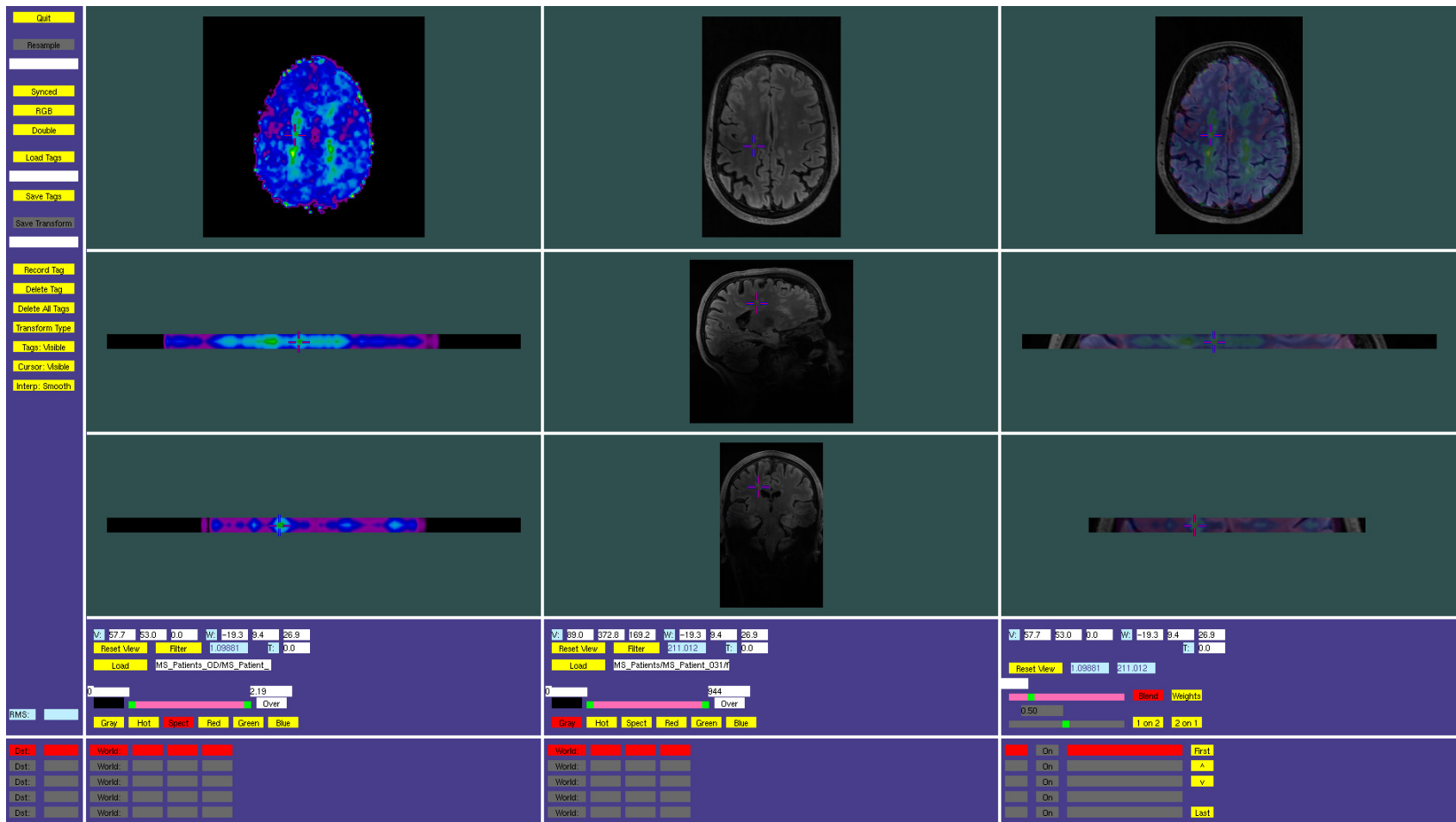


FIGURE 3.22: Ratio of the Ins to the NAA+NAAG metabolic map plotted over the flair image shows metabolic changes even in normal appearing white matter without apparent changes on conventional MRI (e.g. Flair).

Chapter 4

Discussion

The goal of the thesis was to improve spectral properties of MRSI datasets with use of the high-resolution B0 map during postprocessing. The Overdiscrete MRSI reconstruction and the Spectral resolution amelioration by spectral deconvolution were implemented in Matlab. Validation of the methods was performed on the simulation model, phantom data and in vivo data. The performance of the methods was also compared with Signal averaging. Finally, the Overdiscrete MRSI (odMRSI) reconstruction was applied on the clinical data of multiple sclerosis patients.

The odMRSI requires to interpolate MRSI data to a high resolution B0 map and then, the high-resolution B0 map specify how much the sub-voxel spectra should be frequency shifted. The key point of this method is the fact that after the interpolation, the noise is correlated and the different shift of the sub-voxel spectra, which belong to the same MRSI voxel, destroy noise correlation and after the averaging of the sub-voxel spectra, increase the SNR. To destroy noise correlation the B0 map can be replaced by random numbers, which also brings the increase of the SNR and high-resolution B0 map is not necessary. Another way is using the shift map generated by the LCmodel, interpolate it to a higher resolution and use this information in the odMRSI.

SPREAD uses the high-resolution B0 map to simulate the distortion signals, called the lineshape profiles, which caused line broadening and lineshape distortions. The high resolution of the lineshape profiles is lower by the simulated MRSI acquisition to the resolution of the MRSI dataset. Then spectral deconvolution can be performed.

After applying the odMRSI a significant SNR increase and a negligible FWHM change was found. For the simulation model, the SNR increase was in the range between +40% up to +100%. For the phantom data the increase was between +50% and +150%. For the in vivo data, the increase of the SNR was around +100%. Kirchner et al. [6] reported the SNR increase after odMRSI depending on the vector size from +40% up to +210%. The increase

of the FWHM was in all three cases around 5%, while Kirchner et al reported a decrease of the FWHM.

The performance of SPREAD was quantitatively evaluated only on the simulated data. The presence of the noise in the data limits the performance of the SPREAD which was shown on the phantom data, where poor performance was immediately apparent. The results from simulations showed that the Wiener-Gaussian filter increases the SNR (+90%) and the FWHM (+25%) while the following deconvolution lowers the increase for both parameters, the SNR (to +40%) and the FWHM (to +20%). Dong and Peterson [7] reported the change of the FWHM -20% for the phantom measurement, however, the data had much higher SNR. This is a very unusual situation and hence these results can not be translated into clinical reality.

4.1 Validation of methods on the simulated data

The results of the odMRSI from the simulated data showed that the increase of the SNR came from the non-homogeneity of the B0 map. There was no difference in terms of the SNR between the odMRSI with the measured and modified B0 map, while the mean of sub-voxels of the modified B0 map was zero, so the modified B0 map represented just the relative shift between the sub-voxels. The highest SNR increase was thus achieved by the odMRSI, with the random B0 map, however, this case had also the highest FWHM values, which lowers spectral resolution. For the SPREAD method, the results showed that the increase of the parameters is strongly influenced by the Wiener-Gaussian filter, but the deconvolution was not able to decrease the FWHM under the initial values.

4.2 Validation of methods on the phantom data

The results from the phantom validation allowed quantitative validation only on the results from the odMRSI reconstruction. The poor performance of the SPREAD was immediately apparent from the results. The results showed for the odMRSI that, the higher resolution of the B0 map does not yield a higher SNR increase. For 16×16 and 32×32 MRSI resolutions, the SNR increase was higher in case of 64×64 resolution of B0 maps than in case of 128×128 B0 maps. Also for the FWHM, the increase was higher in the same cases, which suggests that the FWHM is traded for the SNR. The decrease of the CRLBS of the fitted metabolite was the same for the both resolution of B0 map in

case of the 16×16 MRSI resolution, while in case of the 32×32 MRSI resolution was different only in two metabolites. These findings suggest that the improvement in the SNR does not automatically mean improvement in the CRLBs but the initially low values of CRLBs and relatively high values of the SNR have to be taken in to account.

4.3 Validation of methods on the in vivo data

The statistical comparison confirmed that odMRSI increases the SNR and the FWHM and decreases the CRLBs of the fitted metabolites. The result also confirmed that the highest improvement was brought by the odMRSI with 400×400 resolution of B0 map.

The comparison of the odMRSI with the Signal averaging shown that the odMRSI with the 400×400 B0 map is superior to the Signal averaging of 5 averages in terms of the SNR and CRLBs. However, the improvement of these two parameters is not directly related to the improvement of the metabolic maps, which was demonstrated on the metabolic map of Glu+Gln.

Finally, it was demonstrated that the odMRSI can be also based on a shift map, which is one of the output from the LCModel fit. In this case the LCModel is run twice, once to generate a shift map and the second run is performed together with the odMRSI reconstruction. For such an approach no B0 map is needed so it does not cost any extra acquisition time.

4.4 Limitations and Outlook

The use of the SPREAD is limited by the low SNR. The deconvolution step in the SPREAD method enhance noise in MRSI data. It was shown that in the MRSI data with the low SNR, not even Wiener-Gaussian filtering was able to ensure a desired level of noise for deconvolution. Moreover, the Wiener-Gaussian filtering decrease the spectral resolution in the MRSI data, which is the main aim of SPREAD.

The odMRSI reconstruction increases the spectral SNR but the improvement in the metabolic maps is questionable. Further investigation is necessary if the odMRSI increases the information content of the data or the improvement is just cosmetic. The statistical comparison between odMRSI and Signal averaging was not performed in term of concentration of metabolites in voxels. However, it is possible to match the improvement of the spectral parameters of the Signal averaging and the odMRSI, so comparison in terms

of the metabolic concentrations could be reasonable. Unfortunately this was not carried out because of lack of time. The next step could be to investigate the improvement of the odMRSI based on the shift maps.

The high resolution B0 map are used also in others methods to improve spectral properties such as BSLIM [19] or in the Reconstruction of MRSI used as the high resolution priors [20]. These methods could be implemented and compared with the odMRSI and SPREAD.

Chapter 5

Conclusion

Based on the results from simulations, both methods, the odMRSI and SPREAD, are capable to improve the spectral properties. However, the way, how the information from the high-resolution B0 map is used, is specific for each of them and defined the limits of these methods. The odMRSI is more robust against the low SNR and was tested also on phantom and in vivo data. Finally the odMRSI was applied on the data of a multiple sclerosis patient, but in this case the shift of the spectra was based on the shifts maps from the LCModel, which means that the odMRSI can be applied with no additional acquisition time.

Bibliography

- [1] Malcolm H. Levitt. *Spin dynamics. basics of nuclear magnetic resonance*. 2nd ed. Hoboken, NJ: John Wiley, c2008. ISBN: 978-0-470-51117-6.
- [2] Robin A. De Graaf. *In vivo NMR spectroscopy. Principles and Techniques*. 2nd ed. Hoboken, NJ: John Wiley, c2007. ISBN: 978-0-470-02670-0.
- [3] Lars G. Hanson. "Is quantum mechanics necessary for understanding magnetic resonance?" In: *Concepts in Magnetic Resonance Part A* 32A.issue 5 (2008), pp. 329–340. ISSN: 15466086. DOI: [10.1002/cmr.a.20123](https://doi.org/10.1002/cmr.a.20123). URL: <http://doi.wiley.com/10.1002/cmr.a.20123>.
- [4] Gilbert Hangel. *Accelerated High-Resolution 3D Magnetic Resonance Spectroscopic Imaging In The Brain At 7T*. Doctoral thesis. Vienna, 2015.
- [5] Andrew G Webb, ed. *Magnetic Resonance Technology. Hardware and System Component Design*. New Developments in NMR. The Royal Society of Chemistry, 2016. ISBN: 978-1-78262-359-5.
- [6] Thomas Kirchner, Ariane Fillmer, and Anke Henning. "Mechanisms of SNR and line shape improvement by B₀ correction in overdiscrete MRSI reconstruction". In: *Magnetic Resonance in Medicine* vol. 77.issue 1 (2017), pp. 44–56. ISSN: 07403194. DOI: [10.1002/mrm.26118](https://doi.org/10.1002/mrm.26118). URL: <http://doi.wiley.com/10.1002/mrm.26118>.
- [7] Zhengchao Dong and Bradley S. Peterson. "Spectral resolution amelioration by deconvolution (SPREAD) in MR spectroscopic imaging". In: *Journal of Magnetic Resonance Imaging* vol. 29.issue 6 (2009), pp. 1395–1405. ISSN: 10531807. DOI: [10.1002/jmri.21784](https://doi.org/10.1002/jmri.21784). URL: <http://doi.wiley.com/10.1002/jmri.21784>.
- [8] MATLAB. *version 8.6.0.267246 (R2015b)*. Natick, Massachusetts: The MathWorks Inc., 2015.
- [9] LCModel. *version 6.3-1*. S.W.Provencher, 2015.
- [10] M. Povazan et al. "Automated routine for MRSI data processing". In: *2nd TRANSACT Meeting—Quality Issues in Clinical MR Spectroscopy* (2014), p. 52.

- [11] Mark A. Brown. "Time-domain combination of MR spectroscopy data acquired using phased-array coils". In: *Magn Reson Med* 2004.52 (2004), pp. 1207–13. DOI: [10.1002/mrm.20244](https://doi.org/10.1002/mrm.20244). URL: <http://doi.wiley.com/10.1002/mrm.20244>.
- [12] T. Laudadio et al. "Improved Lanczos Algorithms for Blackbox MRS Data Quantitation". In: *Journal of Magnetic Resonance* 157.2 (2002), pp. 292–297. DOI: [10.1006/jmre.2002.2593](https://doi.org/10.1006/jmre.2002.2593). URL: <http://linkinghub.elsevier.com/retrieve/pii/S1090780702925930>.
- [13] José P. Marques et al. "MP2RAGE, a self bias-field corrected sequence for improved segmentation and T1-mapping at high field". In: *NeuroImage* vol. 49.issue 2 (2010), pp. 1271–1281. ISSN: 10538119. DOI: [10.1016/j.neuroimage.2009.10.002](https://doi.org/10.1016/j.neuroimage.2009.10.002). URL: <http://linkinghub.elsevier.com/retrieve/pii/S1053811909010738>.
- [14] Sohae Chung et al. "Rapid B1 mapping using a preconditioning RF pulse with TurboFLASH readout". In: *Magnetic Resonance in Medicine* (2010), pp. 439–446. ISSN: 07403194. DOI: [10.1002/mrm.22423](https://doi.org/10.1002/mrm.22423). URL: <http://doi.wiley.com/10.1002/mrm.22423>.
- [15] W. Bogner et al. "High-resolution mapping of human brain metabolites by free induction decay 1H MRSI at 7 T". In: *NMR in Biomedicine* vol. 25.issue 6 (2012), pp. 873–882. ISSN: 09523480. DOI: [10.1002/nbm.1805](https://doi.org/10.1002/nbm.1805). URL: <http://doi.wiley.com/10.1002/nbm.1805>.
- [16] B. Strasser et al. "(2+1)D-CAIPIRINHA accelerated MR spectroscopic imaging of the brain at 7T". In: *Magnetic Resonance in Medicine* vol. 78.issue 2 (2017), pp. 429–440. ISSN: 07403194. DOI: [10.1002/mrm.26386](https://doi.org/10.1002/mrm.26386). URL: <http://doi.wiley.com/10.1002/mrm.26386>.
- [17] B. Strasser et al. "Coil combination of multichannel MRSI data at 7 T. MUSICAL". In: *NMR in Biomedicine* vol.26.issue 12 (2013), pp. 1796–1805. ISSN: 09523480. DOI: [10.1002/nbm.3019](https://doi.org/10.1002/nbm.3019). URL: <http://doi.wiley.com/10.1002/nbm.3019>.
- [18] Berkin Bilgic et al. "Fast image reconstruction with L2-regularization". In: *Journal of Magnetic Resonance Imaging* vol.40.issue 1 (2014), pp. 181–191. ISSN: 10531807. DOI: [10.1002/jmri.24365](https://doi.org/10.1002/jmri.24365). URL: <http://doi.wiley.com/10.1002/jmri.24365>.
- [19] I. Khalidov et al. "BSLIM. Spectral Localization by Imaging With Explicit B0 Field Inhomogeneity Compensation". In: *IEEE Transactions on Medical Imaging* vol. 26.issue 7 (2007), pp. 990–1000. ISSN: 0278-0062.

- DOI: 10.1109/TMI.2007.897385. URL: <http://ieeexplore.ieee.org/document/4265751/>.
- [20] Ramin Eslami and Mathews Jacob. "Robust Reconstruction of MRSI Data Using a Sparse Spectral Model and High Resolution MRI Priors". In: *IEEE Transactions on Medical Imaging* vol. 29.issue 6 (2010), pp. 1297–1309. ISSN: 0278-0062. DOI: 10.1109/TMI.2010.2046673. URL: <http://ieeexplore.ieee.org/document/5440903/>.